



A STUDY OF THE BEHAVIOR AND  
MICROMECHANICAL MODELLING OF GRANULAR SOIL

VOLUME I

A CONSTITUTIVE RELATION FOR  
GRANULAR MATERIALS  
BASED ON THE CONTACT LAW  
BETWEEN TWO SPHERES

by

Ricardo Dobry  
and  
Emmanuel Petrakis

Approved  
distribution

Approved  
distribution

DTIC  
JUL 12 1991

Approved for public release; Distribution Unlimited

Prepared under Contract No. AFOSR-89-0350  
United States Air Force  
Office of Scientific Research  
Bolling Air Force Base

Department of Civil Engineering  
Rensselaer Polytechnic Institute  
Troy, NY 12180-3590

May 1991

DISTRIBUTION STATEMENT A  
Approved for public release;  
Distribution Unlimited

91-04779



91 7 11 073

# REPORT DOCUMENTATION PAGE

Form Approved  
OMB No. 0704-0188

Public reporting burden for this collection of information is estimated to average 1 hour per response, including the time for reviewing instructions, searching existing data sources, gathering and maintaining the data needed, and completing and reviewing the collection of information. Send comments regarding this burden estimate or any other aspect of this collection of information, including suggestions for reducing this burden, to Washington Headquarters Services, Directorate for Information Operations and Reports, 1215 Jefferson Davis Highway, Suite 1204, Arlington, VA 22202-4302, and to the Office of Management and Budget, Paperwork Reduction Project (0704-0188), Washington, DC 20503.

<b>1. AGENCY USE ONLY (Leave blank)</b>		<b>2. REPORT DATE</b> May 22, 1991	<b>3. REPORT TYPE AND DATES COVERED</b> Final 1/6/89-5/15/91	
<b>4. TITLE AND SUBTITLE</b> A Study of the Behavior and Micromechanical Modelling of Granular Soil <span style="margin-left: 150px;">Volume I</span>			<b>5. FUNDING NUMBERS</b> Grant AFOSR-89-0350 PR 2302/C1	
<b>6. AUTHOR(S)</b> Emmanuel Petrakis, Ricardo Dobry, Paul Van Laak, Panos Kotsanopoulos, Tang-Tat Ng, and Li Liu				
<b>7. PERFORMING ORGANIZATION NAME(S) AND ADDRESS(ES)</b> Civil Engineering Department Rensselaer Polytechnic Institute Troy, NY 12180-3590			<b>8. PERFORMING ORGANIZATION REPORT NUMBER</b>	
<b>9. SPONSORING / MONITORING AGENCY NAME(S) AND ADDRESS(ES)</b> AFOSR/NA Bldg. 410 Bolling AFB Washington, DC 20332-6448			<b>10. SPONSORING / MONITORING AGENCY REPORT NUMBER</b>  AFOSR - 89-0350	
<b>11. SUPPLEMENTARY NOTES</b>				
<b>12a. DISTRIBUTION / AVAILABILITY STATEMENT</b> Approved for Public Release; Distribution Unlimited			<b>12b. DISTRIBUTION CODE</b>	
<b>13. ABSTRACT (Maximum 200 words)</b> <p>A comprehensive research effort has been conducted on constitutive and micromechanical modelling of granular soil. This includes: 1) the development of a new constitutive relation for granular media based on the contact law between two spheres; 2) an experimental investigation on the stress-strain response of a glass bead material with 46 monotonic and cyclic experiments on hollow cylinder specimens, most of them constant mean stress tests to measure deviatoric response and behavior of initial and subsequent yield loci; and 3) numerical simulations of the behavior of granular media using the discrete element method.</p> <p>The proposed constitutive law captures a number of key aspects of the observed stress-strain behavior of granular soils, and it predicts well the experiments on glass beads. Novel aspects of the proposed model include yield cones parallel to the failure envelope, and a basic relation between the field of elastoplastic moduli and the elastic constants of the material.</p>				
<b>14. SUBJECT TERMS</b> Micromechanics; Constitutive Law; Granular Media; Sand; Yield Surface Distortion; Hollow Cylinder Experiment; Discrete Element Simulations; Plasticity			<b>15. NUMBER OF PAGES</b>	
			<b>16. PRICE CODE</b>	
<b>17. SECURITY CLASSIFICATION OF REPORT</b> Unclassified	<b>18. SECURITY CLASSIFICATION OF THIS PAGE</b> Unclassified	<b>19. SECURITY CLASSIFICATION OF ABSTRACT</b> Unclassified	<b>20. LIMITATION OF ABSTRACT</b> UL	

The report consists of three volumes, as follows:

Volume I: "A Constitutive Law for Granular Materials Based on the Contact Law Between Two Spheres," by R. Dobry and E. Petrakis.

Volume II: "An Experimental Investigation of the Behavior of Granular Media Under Load," by E. Petrakis, R. Dobry, P. Van Laak, and P. Kotsanopoulos.

Volume III: "A Numerical Investigation of the Behavior of Granular Media Using Nonlinear Discrete Element Simulations," by E. Petrakis, R. Dobry, T.-T. Ng, and L. Liu.

# TABLE OF CONTENTS

	<u>Page</u>
LIST OF SYMBOLS	iii
ACKNOWLEDGMENTS	vii
1. INTRODUCTION	1
2. CONTACT MODEL	5
3. STRESS-STRAIN CONSTITUTIVE MODEL FOR GRANULAR MATERIAL	11
3.1 General Case	11
3.2 Case of $\sigma_{xx} = \sigma_{yy}$ and $\tau_{xy} = \tau_{yz} = 0$	13
3.3 Simple Stress Paths	18
3.3.1 Isotropic Compression	18
3.3.2 Deviatoric Monotonic Loading	18
3.4 Program GRANULAW	21
4. APPLICATION TO A GRANULAR MATERIAL COMPOSED OF GLASS BEADS	22
4.1 Experimental Results and Model Parameters	22
4.2 Model Verification	24
4.3 Model Predictions and Comparisons	26
5. DISCUSSION AND CONCLUSIONS	29
REFERENCES	35
TABLES	
FIGURES	



Accession For	
DTIC TAB	<input checked="" type="checkbox"/>
Unannounced	<input type="checkbox"/>
Justification	<input type="checkbox"/>
by	
Distribution/	
Availability Codes	
Dist	Avail and/or Special
A-1	

## LIST OF SYMBOLS

### GREEK LETTERS

$\alpha$	normal relative displacement between two spheres
$\gamma$	engineering shear strain
$\gamma^c$	corrected $\gamma_{\text{oct}}$
$\gamma_{\text{oct}}$	octahedral engineering shear strain
$\gamma'_{\text{oct}}$	normalized $\gamma_{\text{oct}}$
$\gamma_{xy}, \gamma_{yz}, \gamma_{zx}$	engineering shear strains
$\delta$	tangential relative displacement between two spheres
$\delta_x, \delta_y$	x,y components of $\delta$
$\epsilon$	normal strain
$\epsilon_v$	volumetric strain
$\epsilon_{xx}, \epsilon_{yy}, \epsilon_{zz}$	normal strains
$\pi$ -plane	deviatoric plane, octahedral plane
$\sigma$	normal stress
$\sigma_1, \sigma_2, \sigma_3$	principal stresses
$\sigma_m$	mean normal stress
$\sigma_{ml}$	limit value of $\sigma_m$
$\sigma_{xx}, \sigma_{yy}, \sigma_{zz}$	normal stresses
$\nu_s$	Poisson's Ratio of two spheres
$\tau$	shear stress
$\tau^c$	corrected $\tau_{\text{oct}}$

$\tau_{\text{oct}}$	octahedral shear stress
$\tau'_{\text{oct}}$	normalized $\tau_{\text{oct}}$
$\tau_{\text{oct}l}$	$\tau_{\text{oct}}$ corresponding to $\sigma_{ml}$
$\tau_{xy}, \tau_{yz}, \tau_{zx}$	shear stresses
$\phi$	friction angle

#### LATIN LETTERS

a	radius of area of contact area between two spheres
B	$3(1 - \nu_s)/(8G_s)$
$B_t$	bulk modulus
$C_1$	constant
$C_2$	constant
$\vec{D}$	relative displacement vector
$d\vec{\epsilon}$	strain increment vector
$d\vec{\tau}$	shear stress increment vector
$d\tau_n$	normal component of $d\tau$
$d\tau_t$	tangential component of $d\tau$
$d\vec{T}$	tangential force increment vector
$dT_n$	normal component of $dT$
$dT_t$	tangential component of $dT$
$E_0$	volumetric strain ( $= \epsilon_v$ )
$E_1, \dots, E_5$	modified deviatoric strains

$\vec{F}$	contact force vector
$f$	friction coefficient, model parameter
$G_0$	elastic shear modulus
$G_s$	shear modulus of two spheres
$G_{nt}$	elastoplastic shear modulus
$G_{tt}$	"tangential" elastic shear modulus
$H$	elastoplastic stiffness
$H_0$	elastic stiffness
$H_p$	"tangential" elastic stiffness
$\hat{i}$	unit vector in x direction
$\hat{j}$	unit vector in y direction
$K$	radius of circle, tangential contact force
$\hat{k}$	unit vector in z direction
$M$	model parameter
$m$	model parameter
$N$	normal contact force between two spheres
$N_i$	value of $N$ for apex of yield cone
$\hat{n}$	unit normal vector
$Q$	model parameter
$Q_1$	model parameter
$Q_2$	model parameter
$q$	model parameter
$q_1$	model parameter

$q_2$	model parameter
$R$	radius of two spheres
$S_0$	mean normal stress ( $= \sigma_m$ )
$S_1, \dots, S_5$	modified deviatoric stresses
$S_{ji}$	coordinate of apex of cone $i$
$S_{0i}$	coordinate of apex of cone $i$
$T$	tangential contact force between two spheres
$T_x, T_y$	$x, y$ components of $T$
$T_{xi}, T_{yi}$	values of $T_x, T_y$ for apex of yield cone
$\hat{t}$	unit tangent vector
$x$	Cartesian coordinate
$y$	Cartesian coordinate
$z$	Cartesian coordinate

## ACKNOWLEDGMENTS

The authors wish to acknowledge the following people and organizations for their valuable assistance in this study:

The Air Force Office of Scientific Research, and especially Lt. Col. Steven C. Boyce, for their continued support throughout this research.

Prof. Ahmed-W. M. Elgamal of the Dept. of Civil Engineering of RPI, Troy, NY for his stimulating discussions.

Prof. Adel Saada, Chairman of the Dept. of Civil Engineering of Case Western Research University for his help.

Mr. Paul Van Laak, Research Engineer, Dept. of Civil Engineering, RPI, Troy, NY for his stimulating discussions and comments.

Mr. Victor Taboada and Ms. Min Fan, Graduate Students in the Dept. of Civil Engineering of RPI, Troy, NY for their assistance in preparing this document.

## 1. INTRODUCTION

Over the past 30 years considerable attention has been given to the development of constitutive laws for engineering materials (Hill, 1950; Prager, 1955; Mroz, 1967, Dafalias and Popov, 1976; Drucker and Palgen, 1981). Among other formulations, the existing models are based on the theories of elasticity, hypoelasticity, plasticity, and viscoplasticity. Despite the large number of models there has been no consensus within the research community on the best approach. However, the models based on the theory of plasticity or viscoplasticity appear to be the most promising.

Some of the most popular and widely used models for sand have been based on the "cap model" of DiMaggio and Sandler (1971). As versatile as "cap models" may be, they have not been successful in accurately modelling monotonic and cyclic loading conditions.

Similar limitations apply to other models (Baladi and Rohani, 1979), and it can be argued that the existing plasticity models of the "cap" type are only adequate for monotonic loading of isotropic soil. In an effort to overcome this, a variety of constitutive laws have been proposed which incorporate a combination of isotropic and kinematic hardening (Mroz, 1967), either in a two (Dafalias and Popov, 1976), or multiple yield surface context (Mroz, 1967; Lade, 1977). Although these more recent theories represent a considerable advancement over the "cap" models, they too have drawbacks. These include the use of "a priori" hardening rules, and the inability to take into account either the prestraining effect after load reversals or the inherent, elastic anisotropy of the soil. This elastic (inherent) anisotropy which is most significant for anisotropically consolidated sand has been measured in sand by Stokoe and his coworkers (Knox, et al., 1982; Koppermann, et al., 1982), while Dafalias (1979) has discussed its modeling implications. Finally, all of the above existing plasticity models for soils are phenomenological; their formulations depend on the interpretation of the macroscopic results by the researcher and not on micromechanical principles. As such, they are in need of constant refinement when needed for cases very different from the one the model was originally developed and calibrated for.

The current situation in metal plasticity is quite different. Although it is true that modelling of the nonlinear behavior of metals started on a similar phenomenological basis, there has been a later shift toward formulating the metal response with due consideration to basic micromechanical principles. Recently, this has been enhanced by specific experiments and micromechanical (electron microscopy) measurements (Stout, et al., 1985; Helling, et al., 1986). The situation is analogous in the modelling of more complex composite materials, where experiments and micromechanical analytical simulations are combined to create the corresponding constitutive law (Dvorak, 1987; Dvorak, et al., 1988).

Although metal properties are not pressure dependent and their symmetry does not change as much with loading as in soils, the stress-strain behavior of metals and soils is in many respects similar. As a result, most current soil plasticity models are modified versions of popular phenomenological metal models. Notable examples include the Mroz (1967) model for metals and the Prevost (1978) model for undrained loading of clay, as well as the bounding surface model used by Dafalias and Popov (1976) for metals and subsequently adapted to soils by Dafalias and Herrmann (1982). Unfortunately, no plasticity model exists for soil resulting from the combination of specific laboratory experiments and micromechanical principles including numerical simulations of granular arrays.

Recently, the geotechnical groups at the University of Colorado (Klisinski, et al., 1988), US Army WES (Peters, 1988), and University College of London (Arthur, et al., 1988), working together in a concentrated effort, developed a constitutive law which is based on a series of innovative 3-D laboratory experiments performed for this purpose (Alawi, et al., 1988). This was probably the first time that a thorough experimental investigation is performed in Soil Mechanics which attempts to verify widely accepted rules, such as the hardening law, the yield surface shape during loading, the normality rule, etc. The resulting model (Klisinski, et al., 1988) is based on the bounding surface model of Dafalias and Popov (1976) and on the theory of "fuzzy" sets.

A large number of models have been proposed for granular soils, including those just mentioned and others (Petrakis and Dobry, 1986; 1987). Most of the models for sands are included in the Proceedings of the International Workshop on Constitutive Equations for Granular Non-Cohesive Soils (Saada and Bianchini, 1989). However, as pointed out in that workshop by Scott (1989), this growing modelling effort often includes an increasing mathematical complexity unrelated to additional physical insight, including models containing a large number of parameters (as many as 40) without clear physical meaning.

The authors have taken a different approach to the formulation of a constitutive law for dry granular soil. They use as a starting point the micromechanical force-deformation contact law between two spheres representing two grains. There is a clear physical justification for this. A number of key features of the stress-strain behavior of cohesionless soils and other granular materials are clearly related to the internal structure of the medium, typically composed of individual particles that interact only at their contact points. In turn, some of these features are traceable to the force-displacement response at the contact between two grains, while others require consideration of the whole geometrical arrangement of the mass of particles. To this last category belong the phenomena of volumetric change under shear (dilation), the inelastic volumetric changes during isotropic consolidation, the effect of overconsolidation, the tendency to densification under cyclic shear, and the structural anisotropy, typically encountered in granular materials.

Aspects of stress-strain behavior for which a clear counterpart is present in the contact force-displacement response are listed in Table 1.

Seridi and Dobry (1984) and Dobry, et al. (1991) have proposed an incremental elastic-plastic model for the contact force-displacement response, which constitutes a general solution to the problem originally studied by Hertz (1882), Cattaneo (1938), and Mindlin and Deresiewicz (1953). This report proposes a stress-strain relation for granular media based on this contact model.

As discussed in the text, in its present form the model is completely defined by a small number of parameters (as few as 5) having very clear physical meaning and related to failure and small strain soil properties of common use in soil mechanics. In addition, it is in principle possible to relate these macroscopic parameters, through averaging techniques, to basic micromechanical properties of the soil at the contact and particle level (Petrakis and Dobry, 1987). On the other hand, the model as proposed here is clearly incomplete and needs further development, as it does not yet reflect all important phenomena observed in granular soil.

After a description of the contact model, the proposed stress-strain relation is presented for the general case. Then, the model is specialized to the particular case of compression, extension, and/or torsional loading of hollow-cylindrical granular specimens as used in the tests discussed in Volume II of this report. A computer program is developed which implements the model for any stress path corresponding to this testing technique. The predictions of the model are then compared with results of the tests of glass beads specimens included in Volume II. This is closed by a discussion of the results and some conclusions.

## 2. CONTACT MODEL

Figures 1 through 7 summarize some of the main features of the elastic-plastic contact force-displacement model developed by Seridi and Dobry (1984) and Dobry, et al. (1991). Figure 1a sketches the two identical spheres in contact, of radius  $R$ , elastic properties  $G_s$  (shear modulus) and  $\nu_s$  (Poisson's Ratio), and friction coefficient  $f$ . The spheres can be compressed and can slide with respect to each other but cannot rotate. Figures 1b and 1c show the 3-D force space

$$\vec{F} = N\hat{i} + T_x\hat{j} + T_y\hat{k}$$

and the corresponding 3-D relative displacement space

$$\vec{D} = \alpha\hat{i} + \delta_x\hat{j} + \delta_y\hat{k}$$

$N$ ,  $T_x$ , and  $T_y$  are, respectively, the normal and two tangential contact force components, while  $\alpha$ ,  $\delta_x$ ,  $\delta_y$  are the normal and two tangential components of the relative displacements between the spheres' centers. The unit vectors  $\hat{i}$ ,  $\hat{j}$ , and  $\hat{k}$  are parallel to the normal to the contact and to the two tangential directions, respectively.

The yield surfaces of the model in force space are sketched in Fig. 2 for two different load histories. There are always infinite yield surfaces, with all being nested cones parallel to each other. All cones have their axes parallel to  $N$ , and they have an inclination  $f$ . Except for the failure cone of equation

$$T_x^2 + T_y^2 = f^2 N^2,$$

the cones do not pass by the origin. The apex of cone  $i$  has an equation:

$$(T_x - T_{xi})^2 + (T_y - T_{yi})^2 = f^2 (N - N_i)^2.$$

This cone is associated with a value of  $N = N_i$ , which is unique and does not vary during loading. On the other hand, the other two coordinates of the apex,  $T_{xi}$  and  $T_{yi}$ , do depend on the history of loading.

The model hardens in a purely kinematic way, as illustrated in Fig. 2a for a history which consists of increasing  $N$  to a constant value followed by a monotonic increase of  $T = T_x$  (force path OAB). Only elastic displacements occur along OA, but both elastic and plastic displacements occur along force path AB. Figure 2b shows the formation of cones for a case of proportional loading from the origin, which also induces only elastic displacements between the two spheres.

Figure 3 shows the force-displacement curve predicted by the model when only the normal force is increased (that is,  $T_x = T_y = 0$ , path OA in Fig. 2a). The behavior is nonlinear elastic, with the normal stiffness increasing as  $N$  increases (locking behavior). The force-displacement curve follows a power law,

$$\alpha = C_1 N^{2/3} \quad (1)$$

where  $C_1 = \text{constant}$ . One consequence of this that the normal stiffness  $dN/d\alpha$  increases with  $N$ :

$$\frac{dN}{d\alpha} = \frac{1.5}{C_1} N^{1/3} \quad (2)$$

Figure 4 plots the stress-strain relation for tangential path AB in Fig. 2a. The behavior is now of yielding type, with failure (sliding of contact) occurring when  $T = fN$ , and the force-displacement curve is given by the equation:

$$\delta = C_2 N^{2/3} [1 - (1 - \frac{T}{fN})^{2/3}] \quad (3)$$

where  $C_2 = \text{constant}$ . An important consequence of Eq. 3 is that the tangential stiffness at point A of Fig. 2a,  $(dT/d\delta)_{T=0}$  is an increasing function of the value of  $N$ :

$$\left(\frac{dT}{d\delta}\right)_{T=0} = \frac{1.5 f}{C_2} N^{1/3} \quad (4)$$

Figures 5 and 6 present the force-displacement response predicted by the model for several simple force paths, and compares these predictions with those obtained originally by

Mindlin and Deresiewicz (1953). In all cases for which particular solutions are available, including those of Figs. 5 and 6, there has been complete agreement between the model and Mindlin-Deresiewicz results. The hysteresis loop PRSUT predicted for cyclic tangential loading in Fig. 5b, in conjunction with the backbone curve OP, satisfies the criterion proposed by Masing (1926). Figure 7b shows the positions of the yield cones after the more complex force path OABCD in Fig. 7a.

The flow rule of the model follows a modified normality rule and is defined by Eq. 5:

$$\vec{dD} = \frac{dN}{2G_s a} \frac{\hat{k}}{1-\nu_s} + \frac{f dN}{H_0} \hat{n} + \frac{dT_n - f dN}{H} \hat{n} + \frac{dT_t}{H_p} \hat{t} \quad (5)$$

where:

$\hat{n}$ : unit vector normal to the yield circle at the current force point (yield circles are defined by the intersection of the yield cones with  $\pi$ -plane, see Fig. 2a)

$\hat{t}$ : unit vector tangent to the yield circle at the current force point

$$dT_n = d\vec{T} \cdot \hat{n}$$

$$dT_t = d\vec{T} \cdot \hat{t} = (dT^2 - dT_n^2)^{1/2}$$

$$\begin{aligned} d\vec{T} &= dT_n \hat{n} + dT_t \hat{t} \\ &= d\vec{T}_n + d\vec{T}_t \end{aligned}$$

f: coefficient of friction of the material of the spheres

$$a = (BNR)^{1/3}, \text{ with } B = \frac{3(1-\nu_s)}{8 G_s}, \text{ and } a = \text{radius of area of contact}$$

R = radius of the two spheres

$G_s, \nu_s$  = elastic properties of the material of the spheres

$$H_0 = \frac{4 G_s a}{2 - \nu_s} \text{ is the elastic stiffness}$$

$$H = H_0 \left[ 1 - \frac{K}{fN} \right]^{1/3}, \text{ elastoplastic stiffness corresponding to the yield circle of radius } K$$

$$H_p = \frac{8G_s a}{2 - \nu_s} \frac{K}{3fN} / \left[ 1 - \left[ 1 - \frac{K}{fN} \right]^{2/3} \right] \text{ is the tangential elastic stiffness}$$

Equations 1 through 4 are contained in the more general Eq. 5, with the corresponding expressions for the constants  $C_1$  and  $C_2$  being functions of the physical parameters of the spheres,  $R$ ,  $G_s$ ,  $\nu_s$ , and  $f$ .

Three of the terms in Eq. 5 are purely elastic, and one contains a plastic component. The first term is  $d\alpha = dN/[2G_s a/(1 - \nu_s)]$  and corresponds to the nonlinear elastic Hertz law. The second elastic term includes part of the elastic-plastic tangential displacement to the yield circle, and is controlled by the elastic stiffness  $H_0 = 4G_s a/(2 - \nu_s)$ . The third term includes both an elastic and a plastic tangential displacement, both normal to the yield circle, and is controlled by the elasto-plastic stiffness  $H = H_0[1 - K/(fN)]^{1/3}$ . Finally, the fourth term gives the elastic displacement tangent to the yield circle, and is controlled by the stiffness  $H_p = \frac{8 G_s a}{2 - \nu_s} / [1 - (1 - \frac{K}{fN})^{2/3}]$ , derived by Seridi and Dobry (1984).

Of particular interest is the elasto-plastic third term in Eq. 5. It is clear that a modified version of the usual normality rule valid for many pressure-independent materials (e.g., see Christian and Desai, 1977) is applicable here: the plastic component of  $\vec{dD}$  is parallel to  $\hat{n}$ , the normal to the yield circle, rather than to the normal to the yield conical surface. This is consistent with the fact that at the contact between the two spheres, only the tangential displacement  $\vec{d\delta} = d\delta_x \hat{i} + d\delta_y \hat{j}$  can contain a plastic component, with the normal displacement  $\vec{d\alpha} = d\alpha \hat{k}$  being purely elastic from the Hertz solution.

It is interesting to summarize the parameters of the contact model described by Eqs. 1 through 5 in a way useful to its adaptation to a stress-strain model as discussed in the following sections.

There are four physical parameters corresponding to the properties of the spheres, which characterize the contact model completely:  $R$ ,  $G_s$ ,  $\nu_s$  and  $f$ .

From another viewpoint of more interest here, these four parameters can be replaced by:

- i) The law giving the elastic relation between  $\alpha$  and  $N$ , or between  $dN/d\alpha$  and  $N$ , Eqs. 1-2 and first term of Eq. 5:

$$\frac{dN}{d\alpha} = M \cdot N^m \quad (6)$$

where  $M = 1.5/C_1$  and  $m = 1/3$  in Eq. 2.

- ii) The law giving the elastic-plastic relation between  $T$  and  $\delta$  in Eq. 3, or the tangential stiffness  $(dT/d\delta)_{T=0}$  in Eq. 4, or the elastic second term and the elastic-plastic third term in Eq. 5:

$$\left[ \frac{dT}{d\delta} \right]_{T=0} = Q \cdot N^q \quad (7)$$

where  $Q = 1.5 f/C_2$  and  $q = 1/3$  in Eq. 4. If the formulation of Eq. 7 is adapted, Eq. 3 can be rewritten as follows :

$$\delta = \frac{Q(1-q)}{f} N^{1-q} \left[ 1 - \left( 1 - \frac{T}{fN} \right)^{1-q} \right] \quad (8)$$

- iii) The law giving the elastic tangential stiffness  $(H_p)^{-1}$  in the fourth term of Eq. 5, where

$$H_p = \frac{8 G_s a}{2 - \nu_s} \frac{K}{3 f N} / \left[ 1 - \left( 1 - \frac{K}{fN} \right)^{2/3} \right] \quad (9)$$

where all the terms in the expression are known parameters ( $K$  is the radius of the current yield circle, and for the simplest monotonic loading case it corresponds to the current value of the tangential force,  $K = T$ ).

Therefore, in addition to  $H_p$  in Eq. 9, which will be discussed separately in the next section, the model can be completely characterized by the values of five parameters:  $M$ ,  $m$ ,  $Q$ ,  $q$ , and  $f$ . Note that the monotonic tangential stress-strain curve at constant  $N$  described by Eq. 8 and corresponding to Fig. 4, is completely defined once  $f$ ,  $Q$  and  $q$  are known. This is given by the fact that the value of the elastic-plastic tangential shear moduli:

$$dT/d\delta = Q \cdot N^q (1 - T/fN) = (dT/d\delta)_{T=0} (1 - T/fN) ,$$

corresponding to monotonic loading at point  $B$  in Fig. 2a, is the same at all points in the corresponding cone's surface. That is,  $dT/dN$  at point  $B$  in Fig. 2a is identical to  $(dT/dN)_{T=0} = Q \cdot N_i^q$ , where  $N_i$  is the value of  $N$  corresponding to the apex of the cone passing by point  $B$ .

### 3. STRESS-STRAIN CONSTITUTIVE RELATION FOR GRANULAR MATERIAL

#### 3.1 General Case

The force-displacement contact model described in the previous chapter can be transformed into a stress-strain relation for granular material using modified deviatoric stress and strain spaces. The modified 6-D deviatoric stress space used has one isotropic stress axis  $S_0$  and five deviatoric axes,  $S_1$  to  $S_5$ , defined as follows:

$$\begin{aligned}
 S_0 &= (\sigma_{xx} + \sigma_{yy} + \sigma_{zz})/3 = \sigma_m \\
 S_1 &= (\sigma_{xx} - \sigma_{yy})/3 \\
 S_2 &= [(\sigma_{yy} - \sigma_{zz})^2 + (\sigma_{zz} - \sigma_{xx})^2]^{0.5}/3 \\
 S_3 &= (\sqrt{6}/3) \tau_{xy} \\
 S_4 &= (\sqrt{6}/3) \tau_{yz} \\
 S_5 &= (\sqrt{6}/3) \tau_{zx}
 \end{aligned} \tag{10}$$

where  $\sigma_{xx}$ ,  $\sigma_{yy}$ ,  $\sigma_{zz}$ ,  $\tau_{xy}$ ,  $\tau_{yz}$ ,  $\tau_{zx}$  are the customary normal and shear stresses corresponding to three fixed cartesian axes  $x$ ,  $y$  and  $z$ . In this space, a  $\pi$ -plane is defined by  $S_0 = \text{constant}$ , and it is easy to verify that the magnitude of the octahedral shear stress is the projection of the stress vector on this  $\pi$ -plane:  $\tau_{\text{oct}} = (S_1^2 + S_2^2 + S_3^2 + S_4^2 + S_5^2)^{0.5}$ . Similar to the infinite yield cones in 3-D force space  $(N, T_x, T_y)$  in Fig. 2, there is an infinite number of yield cones in this 6-D space, with equations of the form:

$$\sum_{j=1}^5 (S_j - S_{ji})^2 = f^2 (S_0 - S_{0i}) \tag{10a}$$

where  $f = \tan \phi$  describes the failure envelope of the soil, and  $S_{0i}, S_{1i}, \dots, S_{5i}$  are the coordinates of the apex of the 6-D cone. For the special case in which the loading does not

involve rotation of the principal stress directions, it is possible to come back to a 3-D space, which most conveniently can be defined by the principal stresses  $(\sigma_1, \sigma_2, \sigma_3)$ ; Fig. 8 sketches a couple of the yield cones for this case. Either in 6-D or 3-D space, and the same as in the contact model, the cones move as rigid bodies (purely kinematic strain hardening), with the apex of cone  $i$  always contained in the same  $\pi$ -plane, independently of the history of loading. That is, in 6-D space  $S_{0i}$  is constant and unaffected by the loading history. Also, the same as in the contact model, the yield circles, defined by the intersection of the yield cones with any deviatoric plane ( $\pi$ -plane) are always circles and are never distorted whatever the loading history.

Parallel to the 6-D modified deviatoric stress space there is a modified deviatoric strain space, defined by a volumetric strain axis  $E_0$  and five deviatoric strain axes:

$$\begin{aligned}
 E_0 &= \epsilon_{xx} + \epsilon_{yy} + \epsilon_{zz} = \epsilon_v \\
 E_1 &= 2(\epsilon_{xx} - \epsilon_{yy})/3 \\
 E_2 &= 2[(\epsilon_{yy} - \epsilon_{zz})^2 + (\epsilon_{zz} - \epsilon_{xx})^2]^{0.5}/3 \\
 E_3 &= (\sqrt{6}/3) \gamma_{xy} \\
 E_4 &= (\sqrt{6}/3) \gamma_{yz} \\
 E_5 &= (\sqrt{6}/3) \gamma_{zx}
 \end{aligned} \tag{11}$$

where  $\epsilon_{xx}$ ,  $\epsilon_{yy}$ ,  $\epsilon_{zz}$  are normal strains and  $\gamma_{xy}$ ,  $\gamma_{yz}$ ,  $\gamma_{zx}$  are engineering shear strains. The magnitude of the (engineering) octahedral shear strain is

$$\gamma_{oct} = (S_1^2 + S_2^2 + S_3^2 + S_4^2 + S_5^2)^{0.5}.$$

Similar to the contact model,  $E_0$  is computed from  $S_0$  through a nonlinear elastic relation, and thus  $E_0$  is purely elastic. On the other hand, for any stress increment, the five deviatoric strain components  $E_1$  to  $E_5$  include plastic strains, calculated by means of a flow rule where normality is only observed on the deviatoric plane ( $\pi$ -plane). That is,

the plastic strain increments are normal to the yield circles and not to the yield cones. Flow rules such as this, associative only on the  $\pi$ -plane, have also been allowed for in other constitutive models (e.g., Prevost, 1985).

Once  $E_0$  through  $E_5$  are determined from the model, the three shear strains,  $\gamma_{xy}$ ,  $\gamma_{yz}$ ,  $\gamma_{zx}$  are obtained directly from Eq. 11, and the normal strains,  $\epsilon_{xx}$ ,  $\epsilon_{yy}$ ,  $\epsilon_{zz}$  are calculated from  $E_0$ ,  $E_1$ , and  $E_2$  by inverting a  $3 \times 3$  system of equations (first three lines of Eq. 11).

### 3.2 Case of $\sigma_{xx} = \sigma_{yy}$ and $\tau_{xy} = \tau_{yz} = 0$

A great simplification of the model and a return to 3-D space is obtained for loading histories where  $\sigma_{xx} = \sigma_{yy}$  and  $\tau_{xy} = \tau_{yz} = 0$ . These include all possible laboratory tests that can be done with the triaxial/torsional apparatus on hollow-cylinder granular specimens, such as described in Volume II, provided that the inside and outside pressures are kept the same. In these tests,  $\sigma_{zz}$  = vertical axial stress,  $\sigma_{xx} = \sigma_{yy}$  = cell pressure, and  $\tau_{zx}$  = torsional shear stress. Furthermore, in what follows it will be assumed that a similar behavior is valid for the strains, with normal strains,  $\epsilon_{xx} = \epsilon_{yy}$ , and engineering shear strains,  $\gamma_{xy} = \gamma_{yz} = 0$ .

Therefore, in Eq. 10,  $S_1 = S_3 = S_4 = 0$ , and only three stress components are required:  $S_0 = \sigma_m = \frac{1}{3} (2\sigma_{xx} + \sigma_{zz})$ ,  $S_2 = \sqrt{2} / 3 (\sigma_{zz} - \sigma_{xx})$ , and  $S_5 = \sqrt{6} / 3 \tau_{zx}$ .

These stresses are the counterpart of the three contact forces in Figures 1 and 2 as follows:

<u>Contact Force</u>	<u>Stress</u>
N	$S_0 = \sigma_m = 1/3 (2 \sigma_{xx} + \sigma_{zz})$
$T_x$	$S_2 = \sqrt{2} / 3 (\sigma_{zz} - \sigma_{xx})$
$T_y$	$S_5 = \sqrt{6} / 3 \tau_{zx}$

and the yield cones in this 3-D stress space look identical to and follow the same rules as those of Fig. 2.

The corresponding stress space and yield cones are depicted in Fig. 9. The deviatoric, octahedral or  $\pi$ -plane is defined by the deviatoric coordinates  $\sqrt{2}/3 (\sigma_{zz} - \sigma_{xx})$  and  $\sqrt{6}/3 \tau_{zx}$ , and a vector from the origin O of the  $\pi$ -plane has the magnitude of the octahedral shear stress  $|\vec{\tau}_{oct}| = \tau_{oct}$ :

$$|\vec{\tau}_{oct}| = \tau_{oct} = \frac{1}{3} \sqrt{6(\tau_{zx})^2 + 2(\sigma_{zz} - \sigma_{xx})^2} \quad (12)$$

That is, the position of any stress point in the stress space of Fig. 9 is defined by the position vector  $\vec{\sigma}$  from the origin of the whole stress space:

$$\vec{\sigma} = \frac{\sqrt{2}}{3} (\sigma_{zz} - \sigma_{xx}) \hat{i} + \frac{\sqrt{6}}{3} \tau_{zx} \hat{j} + \sigma_m \hat{k} = \vec{\tau}_{oct} + \sigma_m \hat{k} \quad (13)$$

From the viewpoint of constant mean stress laboratory tests on isotropically consolidated hollow cylindrical specimens of granular material, all stress paths in Fig. 9 are contained in the corresponding  $\pi$ -plane. For example, all monotonic constant mean stress tests correspond to radial stress lines in the  $\pi$ -plane starting from point 0 in the figure and extending to the failure cone:

$$[\sqrt{2}/3 (\sigma_{zz} - \sigma_{xx})]^2 + (\sqrt{6}/3 \tau_{zx})^2 = \tau^2 \sigma_m^2 \quad (14)$$

In the figure, the direction OA corresponds to a compression-extension test in which the axial stress  $\sigma_{zz}$  is increased and the cell pressure  $\sigma_{xx}$  is decreased to maintain  $\sigma_m = 1/3 (2\sigma_{xx} + \sigma_{zz}) = \text{constant}$  (compression test in soil mechanics parlance). The direction OB corresponds to an extension-compression test ( $\sigma_{zz}$  is decreased and  $\sigma_{xx}$  increased; extension test in soil mechanics parlance). Finally, directions OC and OD correspond to purely torsional shear monotonic loading. Oblique directions would correspond to combined axial-torsional tests. The corresponding parallel 3-D strain

space, under the assumption that  $\epsilon_{xx} = \epsilon_{yy}$  and  $\gamma_{xy} = \gamma_{yz} = 0$ , is given by the following three strain coordinates, obtained from Eq. 11 with  $E_1 = E_3 = E_4 = 0$ :

<u>Strain</u>	<u>Corresponding Stress</u>
$E_0 = \epsilon_v = (2 \epsilon_{xx} + \epsilon_{zz})$	$S_0 = \sigma_m = 1/3 (2 \sigma_{xx} + \sigma_{zz})$
$E_2 = 2 \sqrt{2} / 3 (\epsilon_{zz} - \epsilon_{xx})$	$S_2 = \sqrt{2} / 3 (\sigma_{zz} - \sigma_{xx})$
$E_5 = \sqrt{6} / 3 \gamma_{zx}$	$S_5 = \sqrt{2} / 3 \tau_{zx}$

$\epsilon_v = (2 \epsilon_{zz} + \epsilon_{xx})$  is the volumetric strain, while  $2 \sqrt{2} / 3 (\epsilon_{zz} - \epsilon_{xx})$  and  $\sqrt{6} / 3 \gamma_{zx}$  are deviatoric strains. This 3-D strain space is the counterpart of the 3-D displacement space for the contact in Fig. 1c. The deviatoric or octahedral plane in strain space is defined by the deviatoric coordinates  $2 \sqrt{2} / 3 (\epsilon_{zz} - \epsilon_{xx})$  and  $\sqrt{6} / 3 \gamma_{zx}$ , and a position vector from the origin of this octahedral plane has the magnitude  $|\vec{\gamma}_{oct}| = \gamma_{oct}$ :

$$\gamma_{oct} = \frac{2}{3} \sqrt{2 (\epsilon_{zz} - \epsilon_{xx})^2 + 3/2 \gamma_{zx}^2} \quad (14)$$

That is, the location of any strain point in this strain space is defined by a position vector  $\vec{\epsilon}$  from the origin of the whole strain space:

$$\vec{\epsilon} = 2 \sqrt{2} / 3 (\epsilon_{zz} - \epsilon_{xx}) \hat{i} + \sqrt{6} / 3 \gamma_{zx} \hat{j} + \epsilon_v \hat{k} = \vec{\gamma}_{oct} + \epsilon_v \hat{k} \quad (15)$$

The flow rule for the stress-strain model, equivalent to Eq. 5, is:

$$d\vec{\epsilon} = \frac{d\sigma_m}{B_t} \hat{k} + \frac{f d\sigma_m}{G_0} \hat{n} + \frac{d\tau_n - f d\sigma_m}{G_{nt}} \hat{n} + \frac{d\tau_t}{G_{tt}} \hat{t} \quad (16)$$

where the unit vectors  $\hat{k}$ ,  $\hat{n}$  and  $\hat{t}$  have the same meaning as in Eq. 5,  $d\tau_n = d\vec{\tau}_{oct} \cdot \hat{n}$ , and  $d\tau_t = d\vec{\tau}_{oct} \cdot \hat{t}$ .

It is interesting to discuss the parameters of the model, contained in Eq. 16, following the logic used at the end of Chapter 2. The parameters are defined as follows:

- i) The first term of Eq. 16 contains  $B_t = \text{bulk modulus} = d\sigma_m/d\epsilon_v$ , which can be expressed as a power of  $\sigma_m$ , similar to Eq. 6 :

$$B_t = M \cdot \sigma_m^m \quad (17)$$

- ii) The law giving the elastic shear modulus  $G_0 = (d\tau/d\gamma)_{\tau=0}$  and the elastoplastic shear modulus  $G_{nt} = d\tau/d\gamma$  for the second and third terms of Eq. 16, respectively.  $G_0$  can be expressed as a power of  $\sigma_m$ , similar to Eq. 7 :

$$G_0 = Q \cdot \sigma_m^q \quad (18)$$

and

$$G_{nt} = G_0 \left(1 - \frac{\tau_{oc} t}{\Gamma \sigma_m}\right)^q \quad (19)$$

As will be seen later in this volume, the exact expressions of  $G_0$  and  $G_{nt}$  - and especially the value of the power  $q$  - at low values of the confining pressure  $\sigma_m$ , determine the shape of the shear stress-strain curve near failure predicted by the model. There is some evidence in both arrays of spheres (Duffy and Mindlin, 1957) and sands (Seed and Silver, 1972), that at very low pressures the value of  $q$  is larger than at higher pressures. In that case, Eq. 18 is replaced by:

$$\begin{aligned} G_0 &= Q_1 \sigma_m^{q_1} & \text{for} & \quad \sigma_m \leq \sigma_{m\ell} \\ G_0 &= Q_2 \sigma_m^{q_2} & \text{for} & \quad \sigma_m \geq \sigma_{m\ell} \end{aligned} \quad (18a)$$

where  $q_2 < q_1$  and  $Q_2 = Q_1 (\sigma_{m\ell})^{q_1 - q_2}$ . If Eqs. 18a are used, Eq. 19 is replaced by Eqs. 19a and 19b:

$$\begin{aligned} \text{If } \sigma_m \leq \sigma_{m\ell} \\ G_{nt} &= Q_1 \sigma_m^{q_1} \left(1 - \frac{\tau_{oc} t}{\Gamma \sigma_m}\right)^{q_1} \end{aligned} \quad (19a)$$

If  $\sigma_m \geq \sigma_{m\ell}$

$$G_{nt} = Q_2 \sigma_m^{q_2} \left(1 - \frac{\tau_{oct}}{f \sigma_m}\right)^{q_2} \text{ for } \tau_{oct} \leq \tau_{oct\ell}$$

$$G_{nt} = Q_1 \sigma_m^{q_1} \left(1 - \frac{\tau_{oct}}{f \sigma_m}\right)^{q_1} \text{ for } \tau_{oct} \geq \tau_{oct\ell} \quad (19b)$$

where  $\tau_{oct\ell} = f(\sigma_m - \sigma_{m\ell})$ .

- iii) If a strict parallel stress-strain counterpart behavior is accepted with respect to the force-displacement contact model of Eq. 5, the "tangential" elastic shear modulus  $G_{tt}$  in the fourth term of Eq. 16, is given by the rest of the parameters of the stress-strain model, as follows :

$$G_{tt} = \frac{Q(1-q)}{f \sigma_m^{1-q}} \frac{\tau_{oct}}{1 - \frac{G_0}{G_{nt}} \left(1 - \frac{\tau_{oct}}{f \sigma_m}\right)} \quad (20)$$

In that case, only five parameters are needed to completely define the proposed stress-strain constitutive relation:  $M$ ,  $m$ ,  $Q$ ,  $q$  and  $f$ , or eight parameters if  $Q_1$ ,  $Q_2$ ,  $q_1$ ,  $q_2$ , and  $\sigma_{m\ell}$  are specified. The two numbers ( $M$ ,  $m$ ) define the volumetric stress-strain behavior and can be obtained from isotropic consolidation tests; the two numbers ( $Q$ ,  $q$ ) define the variation of  $G_0$  with  $\sigma_m$  and can be obtained from axial or torsional shear loading of soil specimens consolidated to various  $\sigma_m$ ; and  $f = \tan \phi$  can be obtained from monotonic axial or torsional shear tests to failure. The expression for  $G_{tt}$  in Eq. 20, however, needs to be verified experimentally. If the verification disproves Eq. 20, the model is flexible enough to allow a different specification of  $G_{tt}$  consistent with the experimental results. In this case, however, more parameters will be needed in addition to the five (or eight) model parameters just listed.

### 3.3 Simple Stress Paths

It is useful to examine some main aspects of the stress-strain behavior predicted by the model for a couple of simple monotonic stress paths. This is done in this section for isotropic compression and purely deviatoric (constant mean stress) loading.

#### 3.3.1 Isotropic Compression

In this case,  $\sigma_{xx} = \sigma_{yy} = \sigma_{zz} = \sigma_m$  and all  $\tau$ 's are zero. The stress path is located along the  $\sigma_m$  axis in Fig. 9 and all yield cones have their apexes located along this axis. Equation 16 reduces to  $d\vec{\epsilon} = (d\sigma_m/B_t)\hat{k}$  or  $d\epsilon_v = d\sigma_m/B_t = d\sigma_m/(M\sigma_m^m)$ . The integration of this expression gives the relation between confining pressure  $\sigma_m$  and volumetric strain  $\epsilon_v$ :

$$\epsilon_v = \frac{\sigma_m^{1-m}}{M(1-m)} \quad (21)$$

This is a nonlinear elastic relation valid for any history of isotropic loading or unloading. That is, the model predicts only elastic volumetric strains during isotropic compression. For typical values of  $m < 1$ , the shape of the corresponding  $\epsilon_v$  vs.  $\sigma_m$  curve is similar to that of the  $\alpha$  vs.  $N$  curve in Fig. 3.

#### 3.3.2 Deviatoric Monotonic Loading

In this case, the material is first compressed isotropically to  $\sigma_m$ , and then is loaded monotonically to failure by increasing  $\tau_{Oct}$  in a proportional manner while keeping  $\sigma_m$  constant. These are the constant mean stress tests conducted in Volume II. By considering the definition of  $\tau_{Oct}$  in Eq. 12, this can be accomplished by either increasing  $\tau_{zx}$  (torsion test), increasing  $\sigma_{zz}$  while decreasing  $\sigma_{xx}$  (compression test), by increasing  $\sigma_{xx}$  while decreasing  $\sigma_{zz}$  (extension test), or by other combinations of

compression-torsion or extension-torsion. For a given  $\sigma_m$ , the model predicts the same stress-strain relation,  $\tau_{\text{oct}}$  versus  $\gamma_{\text{oct}}$ , for either of these tests. This is a consequence of the basic assumption of the model that the material is initially isotropic under isotropic loading, reflected in the symmetric disposition of the yield cones around the  $\sigma_m$  axis before deviatoric loading starts (Fig. 9). If Eq. 18 with one value of  $q$  is valid for all  $\sigma_m$ , the stress-strain relation is obtained by integrating Eq. 19,  $G_{\text{nt}} = d\tau_{\text{oct}}/d\gamma_{\text{oct}} = G_0(1 - \tau_{\text{oct}}/f\sigma_m)^q = \text{constant}$ , and the result is Eq. 22:

$$\gamma_{\text{oct}} = \frac{f\sigma_m}{G_0(1-q)} \left[ 1 - \left[ 1 - \frac{\tau_{\text{oct}}}{f\sigma_m} \right]^{1-q} \right] \quad (22)$$

In general, for granular media  $q < 1$ , and thus the shape of the  $\tau_{\text{oct}}$  vs.  $\gamma_{\text{oct}}$  curve is similar to the  $T$  vs.  $\delta$  curve in Fig. 4. The value of the failure shear strain is obtained directly from Eq. 22 by setting  $\tau_{\text{oct}} = f\sigma_m$ , and it is  $(\gamma_{\text{oct}})_{\text{failure}} = f\sigma_m/[G_0(1-q)] = f\sigma_m^{1-q}/[G_0(1-q)]$ . Therefore, this predicted failure strain increases as  $\sigma_m$  increases. Equation 22 describes a very mildly nonlinear stress-strain curve up to failure. This is made apparent if the ratio  $G/G_0$  is obtained, where  $G = (\tau_{\text{oct}}/\gamma_{\text{oct}})_{\text{failure}}$  is the secant shear modulus at failure. From Eq. 22,  $G/G_0 = 1 - q$ , which for a typical  $q = 0.5$  is  $G/G_0 \approx 0.5$ .

A more nonlinear  $\tau_{\text{oct}}$  vs.  $\gamma_{\text{oct}}$  curve is obtained if the faster rate of increase of  $G_0$  with  $\sigma_m$  at low  $\sigma_m$  is incorporated into the formulation, and Eq. 19b is integrated for the typical case of  $\sigma_m > \sigma_{m\ell}$ . In that case, the following expression, similar to Eq. 22:

$$\gamma_{\text{oct}} = \frac{f\sigma_m^{1-q_2}}{Q_2(1-q_2)} \left[ 1 - \left[ 1 - \frac{\tau_{\text{oct}}}{f\sigma_m} \right]^{1-q_2} \right] \quad (23)$$

is valid up to a point in the stress-strain curve defined by  $\tau_{\text{oct}l} = f(\sigma_m - \sigma_{ml})$  and  $\gamma_{\text{oct}l} = f \sigma_m [1 - (\sigma_{ml}/\sigma_m)^{1-q_2}] / [Q_2 \sigma_m^{q_2} (1 - q_2)]$ . The expression for the curve above this point is much more complicated than Eq. 23. Of special interest is the following expression for the strain at failure:

$$(\gamma_{\text{oct}})_{\text{failure}} = \frac{f \sigma_m^{1-q_2}}{Q_2 (1 - q_2)} \left[ 1 - \left[ \frac{\sigma_{ml}}{\sigma_m} \right]^{1-q_2} \right] + \frac{f \sigma_{ml}^{1-q_1}}{Q_1 (1 - q_1)} \quad (24)$$

Whether Eq. 22 or the formulation contained in Eqs. 23-24 is used, different  $\tau_{\text{oct}}$  vs.  $\gamma_{\text{oct}}$  curves are obtained for different confining pressures  $\sigma_m$ , with the curves becoming stiffer (higher  $G_0$ ) and stronger (increased  $f \sigma_m$ ) as  $\sigma_m$  goes up. However, there are a couple of ways in which the stress and the strain can be normalized in the model to achieve unique normalized stress-strain curves independent of  $\sigma_m$ .

In the first way, applicable to the case of Eq. 22, a new normalized stress,  $\tau'_{\text{oct}} = \tau_{\text{oct}} / (f \sigma_m)$  and normalized strain  $\gamma'_{\text{oct}} = (G_0 / f \sigma_m) \gamma_{\text{oct}} = (Q / f \sigma_m^{1-q}) \gamma_{\text{oct}}$  are defined. A simple inspection of Eq. 22 reveals that the normalized curve  $\tau'_{\text{oct}}$  vs.  $\gamma'_{\text{oct}}$  is independent of  $\sigma_m$ . A similar normalization is valid for the case of Eq. 23 up to  $\tau_{\text{oct}l}$  but now using  $Q_2$  and  $q_2$ .

The second way is even simpler, and can be applied to either case contained in Eqs. 22 and 23. It is illustrated by the sketch in Fig. 10. If  $\tau_a$  vs.  $\gamma_a$  is the octahedral stress-strain curve corresponding to the confining pressure  $\sigma_m = \sigma_a$ , and  $\tau_b$  vs.  $\gamma_b$  the corresponding curve for  $\sigma_m = \sigma_b$ , with  $\sigma_b > \sigma_a$ , then the portion DE of one of the curves must be identical to the whole other curve AB. This is a direct consequence of the fact that the tangent modulus  $G_{nt}$  is identical for any pair of corresponding points in the two curves (e.g., points F and G in Fig. 10). Therefore, the normalization procedure consists in first finding in curve CE point D of octahedral stress  $\tau_{bD} = f(\sigma_b - \sigma_a)$ ,

thus defining also the corresponding octahedral strain  $\gamma_{bD}$ . Then, for curve CE, the normalized octahedral stress and strain are, respectively,  $\tau_b^c = \tau_b - \tau_{bD}$  and  $\gamma_b^c = \gamma_b - \gamma_{bD}$ . For curve AB, no modification is necessary. The two curves thus modified are plotted together and should coincide.

As will be seen in Chapter 4, these normalization procedures are very useful to integrate the experimental results and use them to verify the model. In particular, the procedure sketched in Fig. 10 constitutes a direct verification of the model's assumption that all yield cones are parallel to the failure surface.

### 3.4 Program GRANULAW

As part of this research, the authors developed computer program GRANULAW (NU (new) stress-strain constitutive LAW for GRANular media), which implements the model for any arbitrary stress path complying with the conditions  $\sigma_{xx} = \sigma_{yy}$  and  $\tau_{xy} = \tau_{yz} = 0$ . This is the case discussed in Section 3.2 and used in the experiments in Volume II.

In GRANULAW, the applied stress components  $\sigma_{xx} = \sigma_{yy}$ ,  $\sigma_{zz}$  and  $\tau_{zx}$  are specified incrementally by the user and are transformed by the program into the deviatoric stress coordinates discussed in Section 3.2. The program computes the corresponding deviatoric strains which are finally converted to the predicted strains  $\epsilon_{xx} = \epsilon_{yy}$ ,  $\epsilon_{zz}$  and  $\gamma_{zx}$ .

Program GRANULAW is used in Section 4.3 to generate model predicted curves corresponding to several stress paths of interest, including those used for the experiments in Volume II.

#### 4. APPLICATION TO A GRANULAR MATERIAL COMPOSED OF GLASS BEADS

In this chapter, the constitutive model described in Section 3 is applied to the glass bead experiments presented in Volume II. First, the parameters of the model are extracted from the appropriate test results, then the model is verified by normalizing some of the test results in the ways suggested in Section 3.3.2, and finally specific test results are simulated using program GRANULAW and the simulations compared with the actual measurements.

##### 4.1 Experimental Results and Model Parameters

Figures 11 to 21 present experimental results from the tests on dry pluviated glass beads reported in Volume II, in a form suitable to the extraction of parameters  $M$ ,  $m$ ,  $Q$ ,  $q$ , and  $f$  of the constitutive model for this material.

Figure 11 reproduces the pressure vs. volumetric strain data measured in the isotropic compression test on a solid cylinder specimen, taken from Fig. 20 of Volume II. The volumetric strains have already been corrected for membrane compliance (see Vol. II for details.) The figure also shows the reasonable agreement between the  $\epsilon_v$  values and the  $3\epsilon_{zz}$  values measured in the same test. A further verification of this corrected pressure vs. volumetric strain curve in Fig. 11 is provided in the same figure by comparison with isotropic compression data from tests on hollow-cylinder specimens.

As no accurate measure of  $\epsilon_v$  was possible below  $\sigma_m = 35$  Kpa, the corrected plot in Fig. 11 corresponds to  $(\sigma_m - 35)$  vs.  $(\epsilon_v - \epsilon_{v35})$ , rather than to the desired  $\sigma_m$  vs.  $\epsilon_v$  curve. Therefore, the fitting of an equation to the data was conducted as part of an overall optimization scheme which also provided a "best estimate" value of the volumetric strain at  $\sigma_m = 35$  Kpa,  $\epsilon_{v35}$ . Finally, the following expression was obtained and is plotted in Fig. 12:

$$\epsilon_v(\%) = 4.203 \cdot 10^{-3} \sigma_m^{0.777} \quad (\sigma_m \text{ in Kpa}) \quad (25)$$

By comparing this expression with Eq. 21 (where  $\epsilon_v$  is not in %), the following values of the model parameters  $M$  and  $m$  are obtained for the glass beads specimens:

$$M = 3.062 \cdot 10^4$$

$$m = 0.223$$

for  $\sigma_m$  in KPa.

Figures 13 to 16 reproduce deviatoric monotonic test results at  $\sigma_m = 138$  KPa and 180 Kpa which could be used to obtain values of  $G_0$  at those pressures, and which thus are useful to produce the model parameters  $Q$  and  $q$ . The figures are also useful in showing the overall consistency of the test results for octahedral strains up to 0.25%, the degree of isotropy of the material during deviatoric loading (perfect isotropy is assumed by the model), and the volumetric strains (dilation) induced by the deviatoric loading (the model assumes no dilation).

Figures 17 to 19 show the technique used to extract the value of the initial tangent modulus  $G_0$  from these tests. The initial, clearly linear part of the  $\tau_{oct}$  vs.  $\gamma_{oct}$  curve, up to  $\gamma_{oct} = 0.01\%$  or  $0.02\%$  depending on the test, was used, with the slope of the fitted least squares straight line giving  $G_0$ . No effort was made to make the straight line go through the origin, as small voltage offsets may be present in the stress and strain measurements. Therefore, the values of  $G_0$  obtained from Figs. 19 to 21 are, respectively,  $5.84 \cdot 10^4$ ,  $5.42 \cdot 10^4$  and  $6.55 \cdot 10^4$  KPa. In addition, in test GB33, during the isotropic consolidation part of the test, small nondestructive deviatoric excursions up to  $\gamma_{oct} = 0.01\%$  were performed and  $G_0$  was obtained using the same least squares technique. All these results for  $G_0$  are summarized in Table 2.

The least squares expression fitted to the data in Table 2 is:

$$G_0 = 3,802 \sigma_m^{0.557} \quad (26)$$

where both  $G_0$  and  $\sigma_m$  are in KPa. Therefore, the model parameters  $Q$  and  $q$  are:

$$Q = 3,802$$

$$q = 0.557.$$

This value of  $q$  is close to the power 0.5 which has been obtained by many authors for sands using resonant column devices and other measurement techniques (e.g., Hardin and Richart, 1963). On the other hand, there is evidence that this power is greater than 0.5 at very small pressures below about 25 KPa ( $\approx$  500 psf). Seed and Silver (1972) obtained a value of about 0.7 from low-pressure tests on a sand, while Duffy and Mindlin (1957) measured as much as 0.8 on arrays of stainless steel spheres at about 10 KPa. The  $q = 0.557$  just obtained in Table 2 was fitted to measurements performed at pressures 35 KPa ( $\approx$  700 psf) or greater. As mentioned previously in Section 3.3.2, this variation in the value of  $q$  between small and large pressures affects significantly the model predictions near failure during deviatoric loading. Therefore, two other sets of model parameters  $Q$  and  $q$  were assumed consistent with all available evidence, as shown in Table 3.

Figures 20 and 21 present results of two monotonic deviatoric tests to failure, corresponding to  $\sigma_m = 138$  KPa. The parameter  $f$  of the model is simply  $(\tau_{\text{oct}})_{\text{failure}}/\sigma_m$ . A value of  $f = 0.39$  was selected, which gives  $(\tau_{\text{oct}})_{\text{failure}} = (0.39)(138) \approx 54$  KPa, located within the experimental range of Fig. 20.

#### 4.2 Model Verification

A number of monotonic deviatoric tests (constant  $\sigma_m$ ) were conducted at  $\sigma_m = 138$  KPa and one test was done at  $\sigma_m = 180$  KPa (Figs. 13 and 15, respectively). A comparison of Figs. 13 and 15 reveals that the stress-strain curves at the two confining pressures are different, as expected, with the curve in Fig. 15 plotting 20-30% higher.

In Figs. 22 and 23, the normalization procedures suggested by the model and discussed in Section 3.3.2 are applied to all compression tests corresponding to these two

different  $\sigma_m$ . It is expected that the normalization should make the plots unique and independent of  $\sigma_m$ .

Figure 22 plots  $\tau'_{oct} = \tau_{oct}/(f \sigma_m)$  versus  $\gamma'_{oct} = (G_0/f \sigma_m) \gamma_{oct}$  for all compression tests at  $\sigma_m = 138$  and 180 KPa. The results are excellent, with all curves defining a narrow band independent of  $\sigma_m$ .

Figure 23 plots the corrected  $\tau_{oct}$ ,  $\tau^c$ , versus the corrected  $\gamma_{oct}$ ,  $\gamma^c$ , for all tests at 138 KPa,  $\tau^c = \tau_{oct}$  and  $\gamma^c = \gamma_{oct}$ . For test GB19 corresponding to 180 KPa,  $\tau^c = \tau_{oct} - (0.39)(180 - 138) = \tau_{oct} - 16.38$  KPa, and  $\gamma^c$  is obtained by moving the origin of the curve as indicated in Fig. 10. Again, the agreement in Fig. 23 is excellent, providing experimental support to the model assumption of parallel yield cones.

Another assumption of the model is the circular shape of the yield cones (Fig. 9), which implies that the material is isotropic after isotropic consolidation (i.e., no material or structural anisotropy). This is clearly a reasonable assumption for the glass beads material, as shown by the more or less unique  $\tau_{oct}$  vs.  $\gamma_{oct}$  curves obtained experimentally in compression, extension, torsion and combined compression-torsion tests (Figs. 13 and 20). Further evidence of this isotropy at small strains is provided by Fig. 24, reproduced from Vol. II, which plots the locus of points of equal  $\gamma_{oct} = 0.03\%$  in the  $\pi$ -plane for various monotonic deviatoric tests. As discussed in Volume II, Figs. 13, 20, and 24 cannot be used as a sufficient proof of the circular shape of the yield surfaces, as these figures constitute plots of equal total strain  $\gamma_{oct}$  rather than of equal tangent modulus  $G_{nt} = d\tau_{oct}/d\gamma_{oct}$ . However, the evidence of Figs. 13, 20, and 24 is certainly consistent with the assumptions of circular yield cones and of initial anisotropy of the material, and a different behavior of these figures would have thrown doubt on the validity of the model for this material. Furthermore, Fig. 24 provides somewhat stronger evidence, as the circle plotted from the experiments could be interpreted as the first yield surface if the assumption was made that the material is elastic and no plastic strains develop for

$\gamma_{\text{oct}} < 0.03\%$ . Arguments in favor of the existence of this "elastic zone," at least as a good first approximation, are: the fact that  $\gamma_{\text{oct}} = 0.03\%$  is of the same order of magnitude as the threshold strain  $\approx 0.01\%$  at which granular materials start to slide and to develop a new geometric arrangement of particles; and the linear stress-strain behavior up to  $\gamma_{\text{oct}} = 0.01\%$  or  $0.02\%$  exhibited by Figs. 17 to 19.

If the circular locus of  $\gamma_{\text{oct}} = 0.03\%$  is interpreted as the first yield surface, then the corresponding probes for  $\Delta\gamma_{\text{oct}} = 0.03\%$  obtained experimentally in Volume I after monotonic prestraining, can also be interpreted as yield surfaces, and their translation and changes in size and shape can be used to prove or disprove the model assumption of pure kinematic strain hardening. Figure 25, reproduced from Volume II, includes plots for these probes before and after monotonic prestraining in compression, extension, and torsion, respectively. The model predicts that the four probes shown in the figure must be circles of the same size. Although this is not entirely true, and both changes in size and distortions can be observed due to prestraining, the assumption of displaced equal size circles can be defended as a first approximation to the real situation. Further development of the model to incorporate these size and shape changes require further research and are outside the scope of this report.

#### 4.3 Model Predictions and Comparisons

In this section, model predictions using the parameters for the glass beads material developed in Section 4.1 are compared with experimental results of specific tests. Unless otherwise stated, the model parameters used are:  $M = 3.062 \cdot 10^{-4}$ ;  $m = 0.223$ ;  $Q = 3,802$ ;  $q = 0.557$ ; and  $f = 0.39$  ( $B_t$  and  $G_0$  in KPa). Program GRANULAW and closed form solutions were used for the model simulations.

Figures 26 and 28 show the comparisons for deviatoric monotonic loading at constant mean stress  $\sigma_0 = 138$  KPa. In Fig. 27, the agreement between model and the

experimental band is good at small strains, but it deteriorates at larger stresses and strains, with the model stress-strain curve being significantly more linear than that measured in the tests. The model fails at a value of  $\gamma_{\text{oct}} = 0.205\%$ , which is clearly too small. This excessive linearity of the stress-strain response in the model was discussed in Section 3.3.2, and a possible explanation mentioned there was the constant value assumed for the parameter  $q$ . If larger values of  $q$  are assumed at low pressures below 25 KPa, as suggested in Table 3, the  $(\gamma_{\text{oct}})_{\text{failure}}$  increases as shown in Table 4, from 0.205% to 0.322%. This would improve considerably the agreement with the experimental results in Fig. 27.

Figure 28 presents the corresponding comparison for volumetric straining (or dilation) for these monotonic deviatoric tests. For the range of  $\gamma_{\text{oct}}$  shown in the figure, the dilation is very small or nonexistent, versus zero dilation predicted by the model.

Figures 29 and 30 include the predicted and measured response during compression triaxial test GB20, where the stresses  $\sigma_{xx} = \sigma_{yy}$  were kept constant at 138 KPa while  $\sigma_{zz}$  was increased to failure. Again, the predicted stress-strain curve in Fig. 29 agrees well with the test at small strains, but the agreement deteriorates at larger strains, with the model curve being too linear and failing too early. Again, use of either Model 2 or Model 3 with variable  $q$  in Table 4 would improve the agreement.

The agreement between predicted and measured volumetric strains is quite good for Test GB20 in Fig. 30 for the range in which the specimen was contractive ( $\gamma_{\text{oct}} < 0.25\%$ ).

Figures 31 and 32 present the results of deviatoric loading experiment GB32, conducted at a constant  $\sigma_m = 138$  KPa. This test started in compression; that is,  $\sigma_{zz}$  was increased and  $\sigma_{xx}$  was decreased; when  $\gamma_{\text{oct}} = 0.25\%$  was reached,  $\sigma_{zz}$  and  $\sigma_{xx}$  were kept constant while the torsional shear stress  $\tau_{zx}$  was increased to failure. The purpose of this test was to verify the prediction of the model for the "tangential" elastic shear modulus  $G_{tt}$  at the point in the stress path where the increase in  $\tau_{zx}$  started (see

Section 3.2 and Eq. 20 for definition of  $G_{tt}$ ). A decrease in modulus when the test switches from compression to torsional is apparent in Fig. 31, and the corresponding values are listed in Table 5. A model simulation was conducted with GRANULAW where a similar constant  $\sigma_m$  test started in compression and then switched to torsion. However, the exact conditions of the test could not be replicated, as the model fails before  $\gamma_{oct} = 0.25\%$ . Therefore, the switch in the model was arbitrarily implemented at  $\tau_{oct} = 35$  KPa. The change in modulus calculated by the model before and after the switch was very small (see Table 5).

Another deviatoric stress path of interest which can be simulated with GRANULAW is a circular path in the  $\pi$ -plane, with the vector  $\vec{\tau}_{oct}$  rotating in a circle while keeping  $\tau_{oct} = |\vec{\tau}_{oct}| = \text{constant}$ . For this case, the model predicts that  $\gamma_{oct}$  does not change and the behavior is elastic, with  $\epsilon_{zz}$  and  $\epsilon_{xx}$  varying sinusoidally and coming back to their initial values at the end of a cycle. Although no circular path experiment was conducted herein on glass bead specimens, Lanier and Zitouni (1989) and Bianchini, et al. (1989) have reported results of similar deviatoric circular stress path experiments on two sands, which essentially confirm the trends just described, thus qualitatively validating the model proposed in this report.

## 5. DISCUSSION AND CONCLUSIONS

The development of the proposed constitutive model and its application to the glass beads experiments, presented respectively in Chapters 3 and 4, have provided considerable insight on the potential of the model to represent the response of a granular soil.

In the first place, it must be recognized that the use of glass bead specimens prepared by dry pluviation is ideal to calibrate the proposed model, or for that matter any model involving yield cones. The high degree of isotropy exhibited by such material when isotropically consolidated (Figs. 11, 13, and 24) after correcting the measured volumetric strains for the effect of membrane compliance, was consistent with the model's prediction of circular cones with vertices along the  $\sigma_m$  axis during isotropic consolidation. The inherent (structural) anisotropy often present in actual soils composed of nonspherical particles and deposited in a gravitational environment will require replacement by noncircular cones (e.g., elliptical ones), which will also require somewhat more complicated flow and hardening rules than those now present in the formulation.

On the other hand, that isotropy made the glass beads an ideal material to use for trying to resolve some main issues before complicating the model further. Those issues and some tentative conclusions are listed below:

1. Validity of the assumption of yield cones parallel to each other and to the failure surface, which comes about from two facts: 1)  $f = \tan \phi$  is constant and independent of  $\sigma_m$  for a wide range of pressures, and 2) the value of the elastoplastic tangent modulus  $G_{nt}$  associated with a given yield cone must correspond to the  $G_0$  at a certain  $\sigma_m \neq 0$ , which means that the apex of the cone cannot be at the origin of the stress space where  $\sigma_m = 0$ . This is a main contribution of the proposed model, as other models typically assume that the apexes of all yield cones are located at the origin of the stress space. For the relatively narrow range of pressures tested ( $\sigma_m = 138$  and 180 KPa) the

hypothesis of yield cones parallel to the failure surface was confirmed (Figs. 22 and 23). On the other hand, the use of a constant value of  $q \approx 0.5$  in Eq. 18 ( $G_0 = Q \cdot \sigma_m^q$ ) clearly predicted deviatoric stress-strain curves that were too linear compared to the measurements (Fig. 27). This demonstrated the sensitivity of the predicted deviatoric stress-strain behavior to the rate of variation of  $G_0$  at very small  $\sigma_m < 25$  KPa, where no measurements were made and where the state of knowledge for all granular materials including soils is very poor. Higher values of  $q$  at these small  $\sigma_m$  produce increasingly nonlinear deviatoric stress-strain curves which approach the measured ones (Table 4). It is clearly possible to postulate a law  $G_0 = G_0(\sigma_m)$  at low  $\sigma_m$  which will predict precisely the measured stress-strain curves to failure.

2. Validity of a flow rule associative only on the  $\pi$ -plane, with the corresponding assumption that no dilation is present during pure deviatoric loading. This assumption proved to be quite good for a wide range of deviatoric strains and stresses, once the measured volumetric changes had been corrected for membrane compliance, and dilation for this material was found to become significant only near failure (Figs. 14, 21, 23, and 32; see also Fig. 45 in Vol. II). As a result, it is clear that the initial volume reduction in the compression triaxial test GB20, up to a large shear stress and a shear strain of about 0.3%, is purely elastic and is the result of the increase in  $\sigma_m$  during the test, as predicted by the model (Figs. 29 and 30). On the other hand, dilation effects do become important at large shear stresses and strains in the material tested (Fig. 21) as well as in granular soils, and the capability to predict this dilation should be a first priority in the further development of the model. This can be handled, in principle, by modifying the flow rule and/or the hardening rule, as done by Prevost (1985). The modification of the hardening rule would involve rotating the yield cones after a strain level has been

reached, thus allowing for dilation to take place. The more desirable alternative would be to modify the flow rule as done by Prevost in this 1985 publication.

3. Validity of assumed elastic stress-strain behavior during circular stress paths in the  $\pi$ -plane (Eq. 16) and of Eq. 20 to predict the corresponding elastic modulus  $G_{tt}$ . Although no circular paths were implemented in the tests presented in Vol. II, similar circular stress paths on two sands reported by Lanier and Zitouni (1989) and Bianchini, et al. (1989) confirm that the deviatoric stress-strain response is essentially elastic as predicted. On the other hand, the results of test GB32 (Fig. 31 and Table 5) suggest that the change in modulus when a deviatoric stress path changes from radial to circular is much greater than suggested by Eq. 20. The incorporation of an alternative expression for  $G_{tt}$  into the model is trivial and can be done easily once the corresponding experimental evidence becomes available.
4. Validity of the assumption of purely elastic volumetric strains during isotropic consolidation (Eqs. 16-17). Although this hypothesis was not tested experimentally in this research, it is certainly an oversimplification, as it ignores the effect of overconsolidation on the volumetric strain behavior of soils. This current deficiency of the model can be readily corrected with the help of a "cap," as done in other models (Roscoe, et al., 1958; DiMaggio and Sandler, 1971; Baladi and Rohani, 1979).
5. Validity of purely kinematic strain hardening rule assumed by the model, and possibility of appearance of distortions in the yield loci/yield cones during deviatoric loading, as predicted on the basis of micromechanical considerations and measurements on metals (see Vol. II). Results such as shown in Fig. 25 indicate that the model's assumption of pure translation of the yield circles without change in size or shape, while good as a first approximation, is not completely correct and may require further refinement. A possible avenue to incorporate these distortions

is the viscoplasticity mathematical formulation presented by Yen (1979) and Yen and Eisenberg (1987), but without the time rate effect and adapted to allow for the influence of  $\sigma_m$  and to incorporate the modified deviatoric stress space of Eqs. 10. In such a model, a distortion correction term  $R_j$  is introduced into Eq. 10a defining the cones. That is,  $S_j - S_{ji}$  in Eq. 10a is replaced by  $S_j - S_{ji} + R_j$ . Another way is the two-parameter model proposed by Voyiadjis and Foroozesh (1990), where the Hill (1950) anisotropy tensor  $M_{ijkl}$  is used as follows:  $F = M_{ijkl} (S_{kl} - \alpha_{kl}) (S_{ij} - \alpha_{ij}) - f^2 (\sigma_m - \sigma_{mi})^2$ . This formulation is shown to have distinct advantages over previous models and can be implemented numerically in the specialized 3-D version of the model used in this volume.

6. Plastic volumetric straining induced by repeated deviatoric loading (densification associated with cyclic loads). Although this subject was not investigated experimentally to any significant extent in Vol. II, it is known to be important in granular soils, it is not included in the current version of the model, and its further development should include rules to allow for this effect.
7. And, finally, the problem of inherent or structural anisotropy, already mentioned, which was not present in the glass beads results analyzed but which is important in sands and other granular soils. This is an important and complicated problem, which is being currently addressed in Plasticity Theory. "Inherent anisotropy" means that the material is anisotropic in its reference state. After plastic flow has occurred, in general, the material ceases to have the anisotropy of the reference state. A very good example of this is the case of rolled steel; in its stress free state, before rolling, the material is isotropic and its behavior could be described by isotropic functions. After the sheet of steel has been subjected to rolling, it may exhibit orthotropic symmetry, and if this is to be the reference state, the material behavior should be described by orthotropic functions with respect to the new

reference state. The case of soil anisotropy is very similar: if the behavior of an anisotropically consolidated sand is to be described, this has to be done with orthotropic functions. In general, simple solutions applied only to the elastic part of the strain, such as proposed by Hardin (1980), are not appropriate. For example, if the tests of Stokoe and his co-workers, already mentioned, are to be taken into account, orthotropic functions are needed for the description of the phenomenon. It is reported by Hill (1950) and Dafalias (1979) that the yield condition must take into account the material symmetries present in the initial (reference) state. The direction of flow is dependent upon those, and the yield surface must take them into account. This not only complicates the expressions of the yield surface considerably, but the implementation of the law as well. For example, according to Dafalias (1979) and Voyiadjis and Foroozesh (1990), the expression for the yield condition of an orthotropic material becomes  $F = H_{ijkl} S_{ij} S_{kl}$ , where  $H_{ijkl}$  is a fourth rank tensor which depends on the material symmetry and the plastic strain. Despite its obvious complexity, the plasticity of initially anisotropic materials can be taken into account in a number of ways for the cases of transverse isotropy and orthotropy. The case of transverse isotropy is very common in the mechanics of composite materials (Dvorak and Bahei-El Din, 1982), and is handled with the aid of four stress "pseudo-invariants" which take into account the symmetries of the material. In the case of soils, Dafalias (1986), Dafalias and Herrmann (1986), and Anandarajah and Dafalias (1986) have proposed a general plasticity model which has been applied to model isotropic and anisotropic clay in undrained condition. The case of drained loading of sand is more complex, since its behavior is pressure dependent and its material symmetry gets affected by variations in the mean stress  $\sigma_m$ .

In summary, since the model proposed for granular media is founded on the contact law between two spheres, it captures a number of key aspects of the stress-strain behavior of granular soils (see Table 1). Furthermore, it contains a small number of parameters with clear physical meaning which can be readily determined in the laboratory. It also contains some novel aspects (parallel yield cones, and relations between elastoplastic behavior and the elastic small strain constants of the medium) which provide significant new physical insight. In addition, the fact that these elastic small strain constants determining the rate at which plastic flow takes place, can in principle be determined from micromechanical considerations or measured in situ by geophysical techniques, may be potentially significant in both conceptual and practical terms. On the other hand, the model requires further development in the areas 1 through 7 listed above. The implementation of some of these changes is very easy, while others will require a longer analytical and experimental research effort.

## REFERENCES

- Alawi, M. M., S. Sture, and H.-Y. Ko (1988). "True Triaxial and Directional Shear Cell Experiments on Dry Sand," US Army Corps of Engrs. Waterways Experiment Station Report.
- Anandarajah, A., and Y. F. Dafalias (1986). "Bounding Surface Plasticity. III: Application to Anisotropic Cohesive Soils," *J. Eng. Mechanics* 112(12):1292-1318, December.
- Arthur, J. R. F., F. Cutler, T. Dunstan, J. Ford, D. A. Leavell, J. F. Peters, and J. R. Pulsford (1988). "Design Development and Operation of an Advanced Directional Shear Cell," US Army Corps of Engineers Waterways Experiment Station Report.
- Baladi, G. Y., and B. Rohani (1979). "Elastic-Plastic Model for Saturated Sand," *ASCE, J. Geotechnical Eng. Div.* 105(GT4):465-480, April.
- Bianchini, G., P. Puccini, and A. Saada (1989). "Test Results," pp. 89-97, In: Constitutive Equations for Granular Non-Cohesive Soils, A. Saada and G. Bianchini (eds.), Proc. Intl. Workshop, Cleveland, 22-24 July 1987, A. A. Balkema Publishers, Rotterdam, The Netherlands.
- Cattaneo, C. (1938). "Sul contatto di due corpi elastici," *Atti Acad. Naz. Lincei Rc.* 27(6):342-348, 434-436, 474-478.
- Christian, J. T., and C. S. Desai (1977). "Constitutive Laws for Geologic Media," Chapter 2 of Numerical Methods in Geotechnical Engineering, C. S. Desai and J. T. Christian (eds.), McGraw-Hill, New York.
- Dafalias, Y. F., and E. Popov (1976). "Plastic Internal Variables Formalism of Cyclic Plasticity," *J. Appl. Mechanics*, pp. 645-651, December.
- Dafalias, Y. (1979). "Anisotropic Hardening of Initially Orthotropic Materials," *ZAMM* 59:437-516.
- Dafalias, Y. F., and L. R. Herrmann (1982). "Bounding Surface Formulation of Soil Plasticity," Proc. Intl. Symp. on Soils Under Cyclic and Transient Loading, G. Pande and O. C. Zienkiewicz (eds.), Wiley, London, UK, pp. 253-282.
- Dafalias, Y. F. (1986). "Bounding Surface Plasticity. I: Mathematical Foundation and Hypoplasticity," *J. Eng. Mechanics* 112(9):966-987.
- DiMaggio, F. L., and I. S. Sandler (1971). "Material Models for Granular Soils," *J. Eng. Mechanics* 97(EM3):935-950, June.
- Dobry, R., T.-T. Ng, E. Petrakis, and A. Seridi (1991). "A General Model for the Contact Law Between Two Rough Spheres," *ASCE, J. Engineering Mechanics* 117(6):1365-1381, June.
- Drucker, D. C., and L. Palgen (1981). "On Stress-Strain Relations Suitable for Cyclic and Other Loading," *J. Appl. Mechanics*, pp. 479-485, September.

- Duffy, J., and R. D. Mindlin (1957). "Stress-Strain Relations of a Granular Medium," Trans. ASME, J. Appl. Mech., pp. 585-593, December.
- Dvorak, G. J., and Y. A. Bahei-El-Din (1982). "Plasticity Analysis of Fibrous Composites," J. Appl. Mechanics 49:327-335, June.
- Dvorak, G. J. (1987). "Plasticity of Fibrous Composites," Civil Eng. Dept., Rensselaer Polytechnic Institute, Troy, NY, Report to US ARO.
- Dvorak, G. J., Y. A. Bahei-El-Din, Y. Macheret, and C. H. Liu (1988). "An Experimental Study of Elastic-Plastic Behavior of a Fibrous Boron Aluminum Composite," Civil Eng. Dept., Rensselaer Polytechnic Institute, Troy, NY, Report to ONR.
- Hardin, B. O., and F. E. Richart, Jr. (1963). "Elastic Wave Velocities in Granular Soils," Proc. ASCE, J. Soil Mech. & Found. Div. 89(SM-1):33-65, February.
- Hardin, B. O. (1980). "Discussion to 'Anisotropic Shear Modulus due to Stress Anisotropy' by S. K. Roesler," ASCE, J. Geotechnical Eng. Div. 106(GT8):956-958, August.
- Hertz, H. (1882). "Ueber die Berührungsfester Elastischer Körper," J. reine angew. Math. 92:156-171.
- Hill, R. (1950). The Mathematical Theory of Plasticity, Oxford University Press, London, UK.
- Klisinski, M., S. Sture, K. Runesson, and H. K. Ko (1988). "Incremental Constitutive for Cohesionless Granular Materials Based on Fuzzy Sets," Proc. 7th ASCE-EMD Specialty Conf., Blacksburg, VA, p. 150.
- Knox, D. P., K. H. Stokoe, and S. E. Koppermann (1982). "Effects of State of Stress on Velocity of Low Amplitude Shear Waves Propagating Along Principal Stress Directions in Dry Sand," Geotechnical Eng. Rept. GR82-23, Univ. of Texas-Austin.
- Koppermann, S. E., K. H. Stokoe, and D. P. Knox (1982). "Effect of State of Stress on Velocity of Low Amplitude Compression Waves Propagating Along Principal Stress Directions in Sand," Geotechnical Eng. Rept. GR82-22, Univ. of Texas-Austin.
- Lade, P. V. (1977). "Elastoplastic Stress-Strain Theory for Cohesionless Soil with Curved Yield Surfaces," Intl. J. Solids Structures 13:1019-1035.
- Lanier, J., and Z. Zitouni (1989). "Development of a Data Base Using the Grenoble True Triaxial Apparatus," pp. 47-58, In: Constitutive Equations for Granular Non-Cohesive Soils, A. Saada and G. Bianchini (eds.), Proc. Intl. Workshop, Cleveland, 22-24 July 1987, A. A. Balkema Publishers, Rotterdam, The Netherlands.
- Masing, G. (1926). "Eigenspannungen und Verfestigung beim Messing," Proc. 2nd Intl. Cong. Appl. Mechanics, pp. 332-335.
- Mindlin, R. D., and H. Deresiewicz (1953). "Elastic Spheres in Contact Under Varying Oblique Forces," ASME, J. Applied Mechanics, pp. 327-344, September.

- Mroz, Z. (1967). "On the Description of Anisotropic Workhardening," *J. Mech. Phys. Solids* 15:163-175.
- Peters, J. F. (1988). "Kinematic Hardening Under Jump Rotations," *Proc. 7th Eng. Mechanics Conf., Blacksburg, VA*, p. 207.
- Petrakis, E., and R. Dobry (1986). "A Self Consistent Estimate of the Elastic Constants of a Random Array of Equal Spheres with Application to Granular Soil Under Isotropic Conditions," *Civil Eng. Dept., Rensselaer Polytechnic Institute, Troy, NY*, Rept CE-86-04.
- Petrakis, E., and R. Dobry (1987). "Micromechanical Modeling of Granular Soil at Small Strain By Arrays of Elastic Spheres," *Civil Eng. Dept., Rensselaer Polytechnic Institute, Troy, NY*, Rept. CE-87-02.
- Prager, N. (1955). "The Theory of Plasticity: A Survey of Recent Achievement," *Proc. Inst. Mech. Eng.* 169:41-57, London, UK.
- Prevost, J. H. (1978). "Anisotropic Undrained Stress-Strain Behavior of Clays," *ASCE, J. Geotechnical Eng. Div.* 104(GT8):1075-1090, August.
- Prevost, J. H. (1985). "A Simple Plasticity Theory for Frictional Cohesionless Soils," *Soil Dynamics & Earthquake Eng.* 4(1):9-17.
- Roscoe, K. H., A. N. Schofield, and C. P. Wroth (1958). "On the Yielding of Soils," *Geotechnique* 9:22-53.
- Saada, A., and G. Bianchini (eds.) (1989), Constitutive Equations for Granular Non-Cohesive Soils, *Proc. Intl. Workshop, Cleveland, 22-24 July 1987*, A. A. Balkema Publishers, Rotterdam, The Netherlands.
- Scott, Ronald F. (1989) "Constitutive Relations for Soil: Present and Future," pp. 723-725, In: Constitutive Equations for Granular Non-Cohesive Soils, A. Saada and G. Bianchini (eds.), *Proc. Intl. Workshop, Cleveland, 22-24 July 1987*, A. A. Balkema Publishers, Rotterdam, The Netherlands.
- Seed, H. B., and M. L. Silver (1972). "Settlement of Dry Sands During Earthquakes," *J. Soil Mechanics & Foundations Div.* 98(SM4):381-397, April.
- Seridi, A., and R. Dobry (1984). "An Incremental Elastic-Plastic Model for the Force-Displacement Relation at the Contact Between Two Spheres," *Dept. of Civil Eng., Rensselaer Polytechnic Institute, Troy, NY.*, Rept. CE-84-06.
- Voyiadjis, G. Z., and M. Fooroozesh (1990). "Anisotropic Distortional Yield Model," *ASME, J. Appl. Mechanics* 57:537-547.
- Yen, C. F. (1979). "On the Theory of Cyclic Viscoplasticity," *Ph.D. Dissertation, University of Florida, Gainesville, FL.*
- Yen, C. F., and M. A. Eisenberg (1987). "The Role of a Loading Surface in Viscoplasticity Theory," *Acta Mechanica* 69:77-96.

TABLE 1

Parallel Behavior Between Stress-Strain Response of Granular Media and Force-Displacement Response at Contact Between Two Particles

<u>Granular Material</u>	<u>Contact Between Two Particles</u>
Yielding and failure under shear stress	Yielding and failure under tangential force
Locking under normal stress	Locking under normal force
Tangent shear modulus increases with normal stress	Tangential stiffness increases with normal force
Shear strength proportional to normal stress	Tangential strength proportional to normal force
Masing criterion good approximation for cyclic shear-stress shear-strain response of isotropically consolidated material	Masing criterion rigorously valid for cyclic tangential force-tangential displacement response at constant normal force
Secant cyclic shear modulus decreases with increasing cyclic shear strain	Secant cyclic tangential stiffness decreases with increasing cyclic tangential displacement
Hysteretic damping ratio increases with increasing cyclic shear strain	Hysteretic damping ratio increases with increasing tangential displacement

TABLE 2

Fitting of Equation  $G_0 = Q \cdot \sigma_m^q$  to Measured Results on  
Glass Bead Specimens

$\sigma_m$ (KPa)	$G_0$ ( $10^4$ KPa)			
	Test GB33	Test GB19	Other Tests	Equation 26*
35	2.55	----	-----	2.75
70	4.55	----	-----	4.05
105	5.35	----	-----	5.08
138	5.65	----	5.42 to 5.84	5.91
180	----	6.55	-----	6.86

\* Equation 26:  $G_0 = 3,802 \sigma_m^{0.557}$  (KPa).

TABLE 3

Model Parameters Used for Equation

$$G_0 = Q \sigma_m^q, \text{ Glass Bead Specimens}$$

( $G_0$  and  $\sigma_m$  in KPa)

$\sigma_{m\ell}$	Below $\sigma_{m\ell}$		Above $\sigma_{m\ell}$	
	$Q_1$	$q_1$	$Q_2$	$q_2$
No $\sigma_{m\ell}$ , Constant $Q$ and $q$	3,802	0.557	3,802	0.557
25 KPa	2,400	0.70	3,802	0.557
25 KPa	1,740	0.80	3,802	0.557

TABLE 4

Failure Strains Predicted by Model for Various Values of  $q_1$ :  
Monotonic Deviatoric Loading with  $\sigma_m = 138$  KPa

Model	$q_1$ (for $\sigma_m < 25$ KPa)	$q_2$ (for $\sigma_m > 25$ KPa)	$(\gamma_{\text{oct}})_{\text{failure}}^{(*)}$
1	0.557	0.557	0.205%
2	0.70	0.557	0.251%
3	0.80	0.557	0.322%

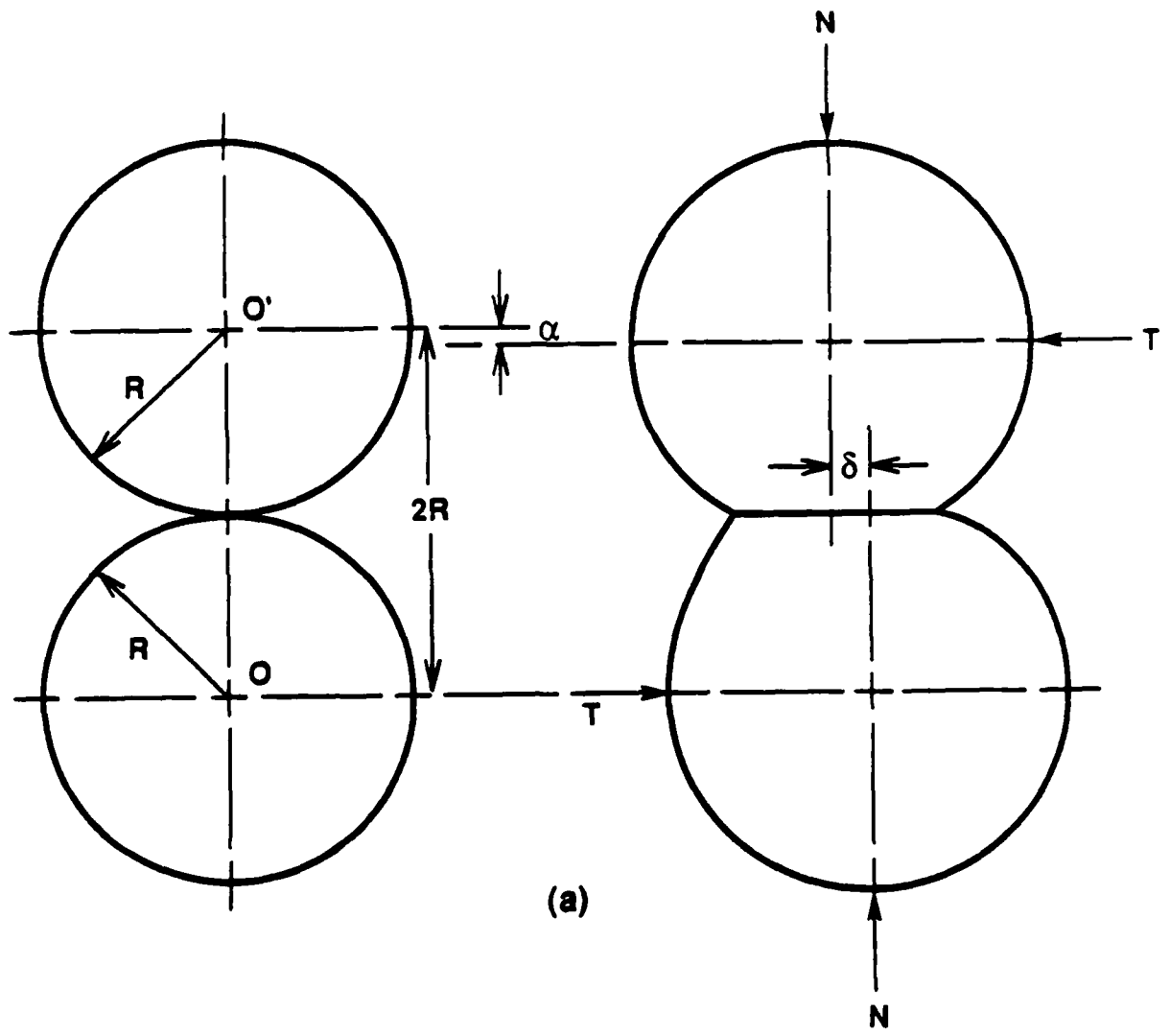
\* $(\gamma_{\text{oct}})_{\text{failure}}$  calculated with Eq. 24.

TABLE 5

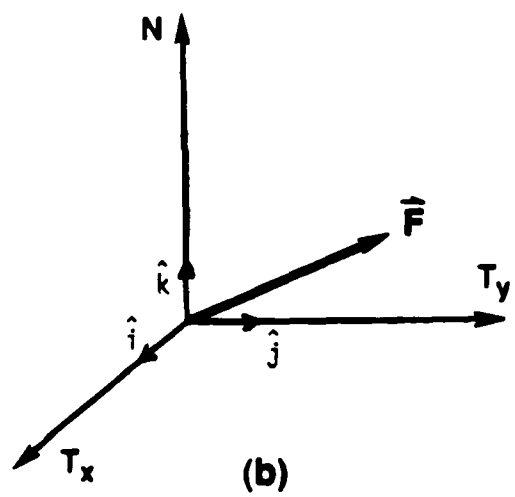
Predicted and Measured Changes from  $G_{nt}$  to  $G_{tt}$  During Deviatoric Loading:

Compression and Torsion Test GB32 at  $\sigma_m = 138$  KPa

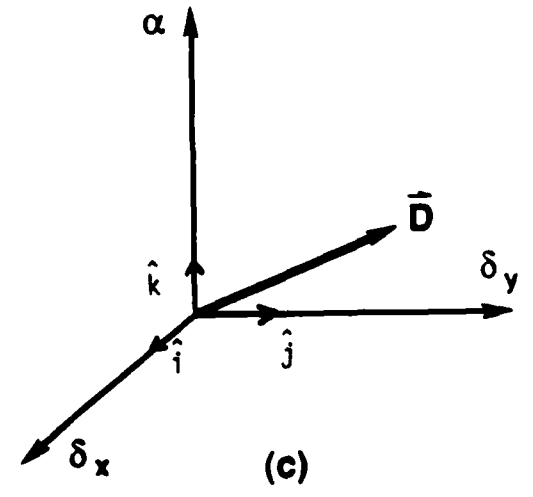
	Place of Switch Compression to Torsion	$G_{nt}$	$G_{tt}$
Model	$\tau_{oct} = 35$ KPa	$3.41 \cdot 10^4$ KPa	$3.15 \cdot 10^4$ KPa
Experiment	$\gamma_{oct} = 0.25\%$ $\tau_{oct} \approx 50$ KPa	$0.99 \cdot 10^4$	$0.23 \cdot 10^4$



(a)



(b)



(c)

Figure 1. (a) Identical elastic rough spheres in contact under normal and tangential forces; (b) contact force space; (c) relative displacement space.

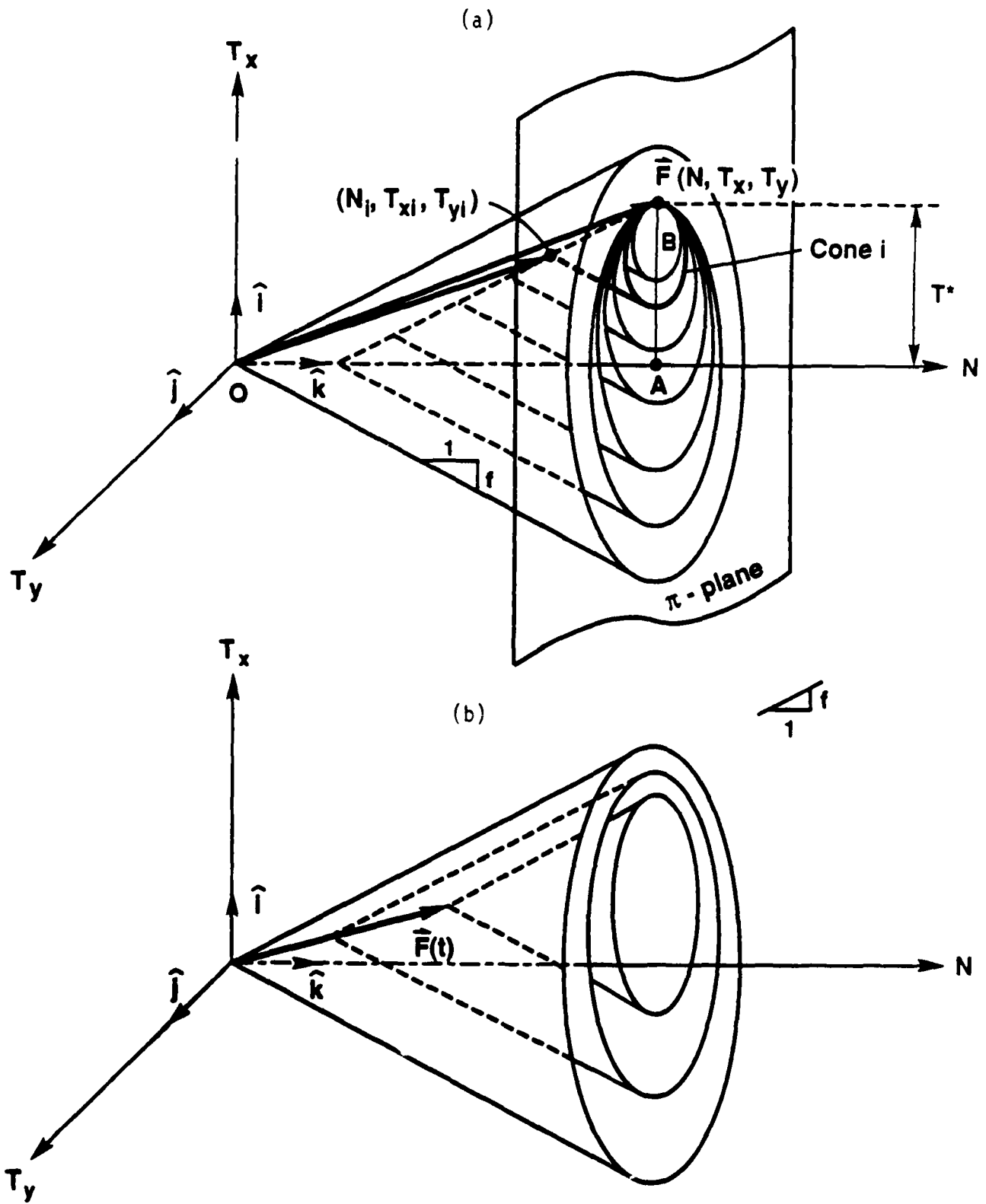


Figure 2. (a) Elastic-plastic contact model, yield cones,  $\pi$ -planes, and yield circles; (b) creation of yield cones for increasing  $N$  and elastic force path ( $dT/dN < f$ ).

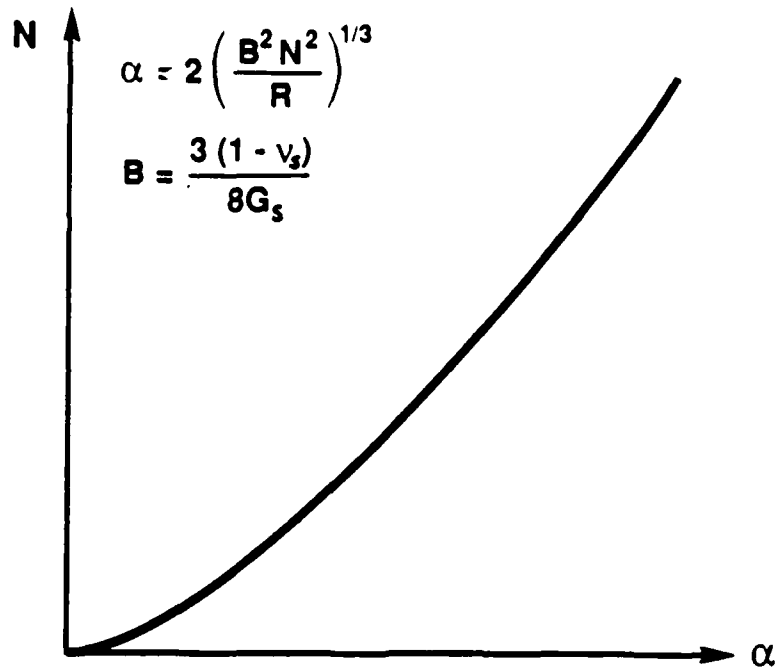


Figure 3. Normal force-displacement nonlinear elastic response in the absence of tangential forces.

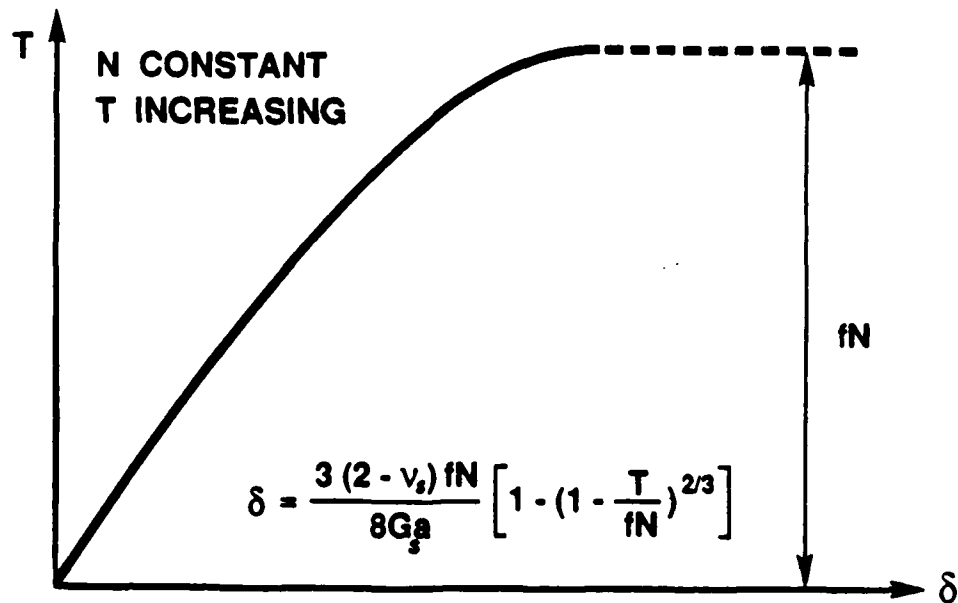


Figure 4. Tangential force-displacement curve for  $N$  constant,  $T = T_x$  increasing, and  $T_y = 0$ .

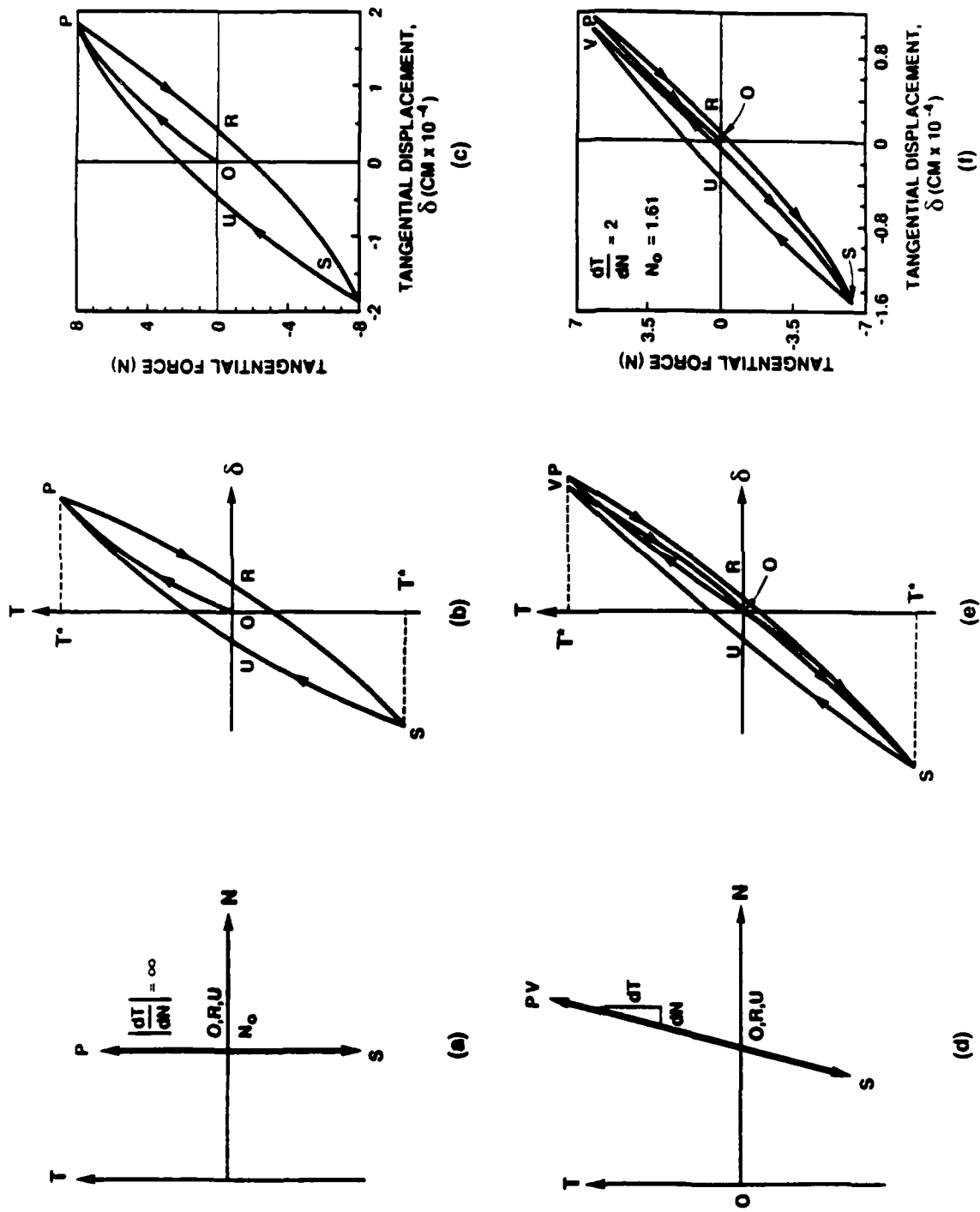


Figure 5. (a) Force path for oscillating tangential force and  $N$  constant ( $|dT/dN| = \infty$ ); (b) corresponding force-displacement loop from Mindlin and Deresiewicz (1953); (c) numerically calculated force-displacement loop for quartz spheres using contact model; (d) force path for oscillating tangential force and  $f < |dT/dN| < \infty$ ; (e) corresponding force-displacement loop from Mindlin and Deresiewicz (1953); and (f) numerically calculated force-displacement loop for quartz spheres using contact model.

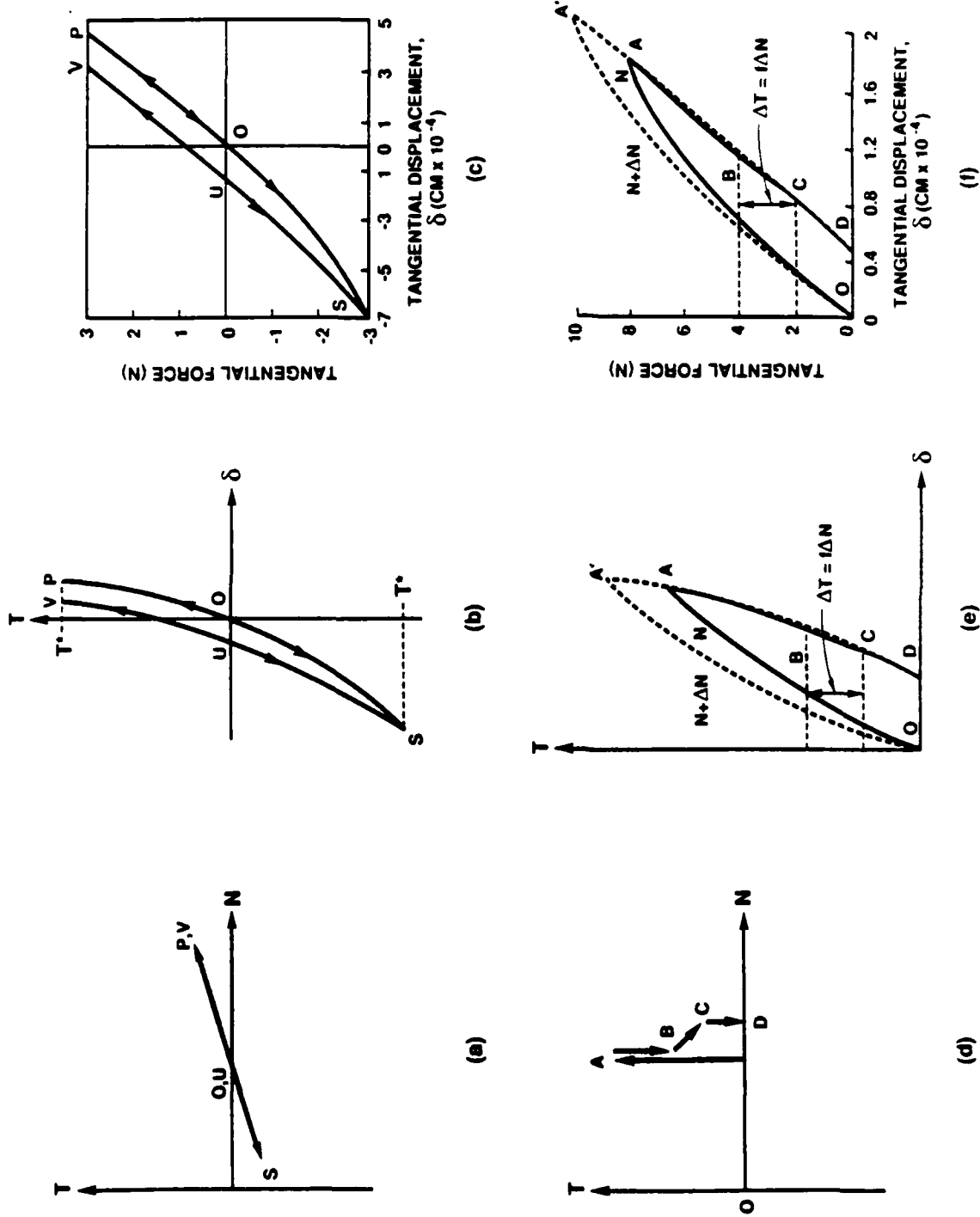


Figure 6. (a) Force path for oscillating tangential force and  $|dT/dN| < f$ ; (b) corresponding nonlinear elastic force-displacement response from Mindlin and Deresiewicz (1953); (c) numerically calculated force-displacement curve for quartz spheres using contact model; (d) force path considered by Mindlin and Deresiewicz (1953); (e) corresponding force-displacement response from Mindlin and Deresiewicz (1953); and (f) numerically calculated force-displacement response for quartz spheres using contact model.

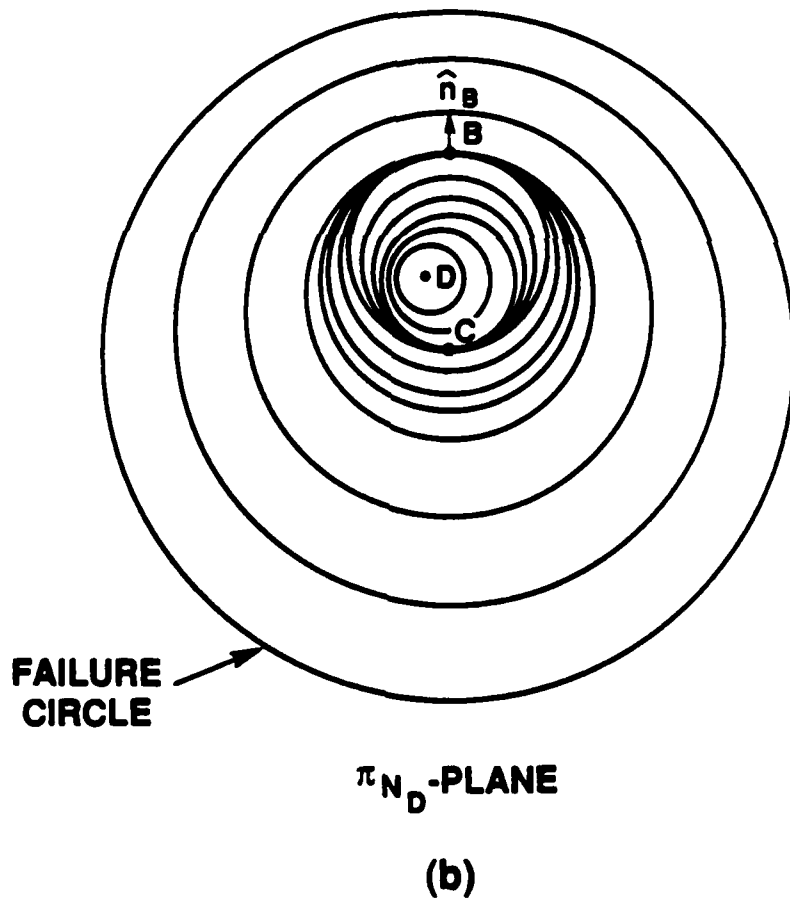
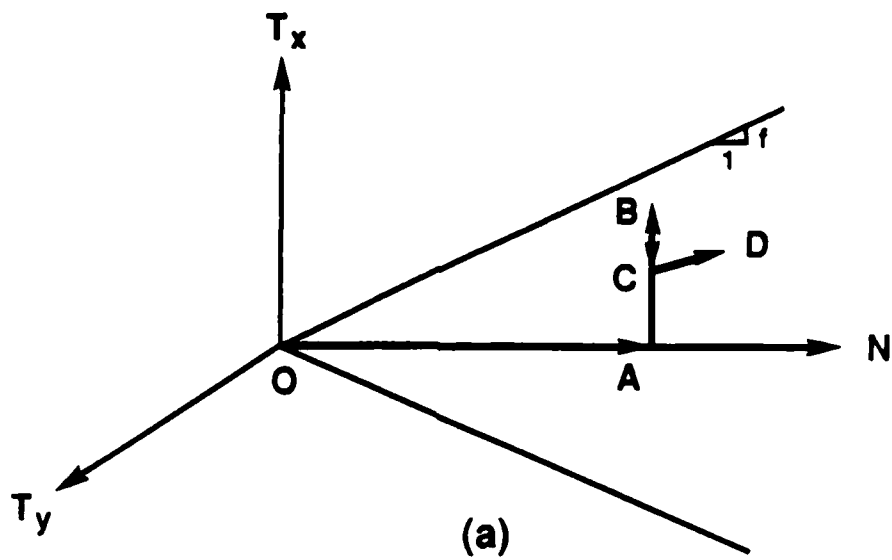


Figure 7. Generation of two groups of yield cones of the first kind and two groups of the second kind in contact model by load path OABCD.

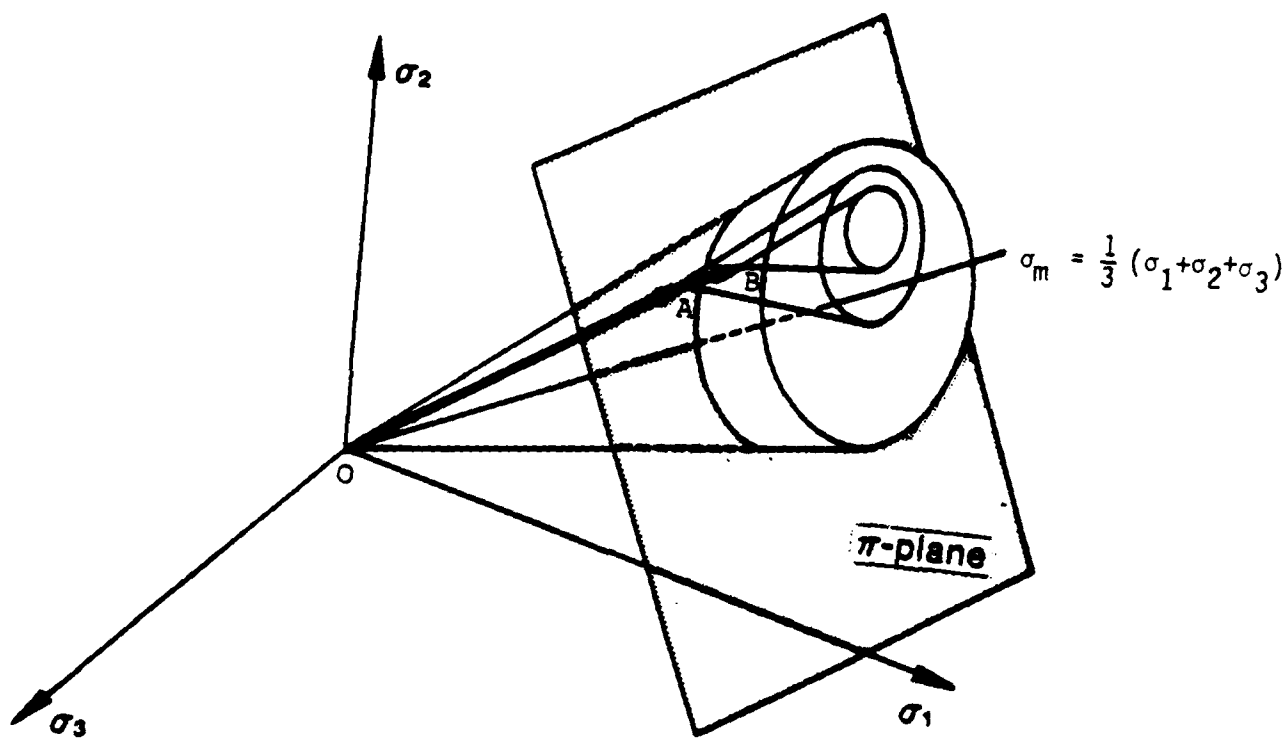


Figure 8. Yield cones,  $\pi$ -planes and yield circles of proposed stress-strain model in principal stress space.

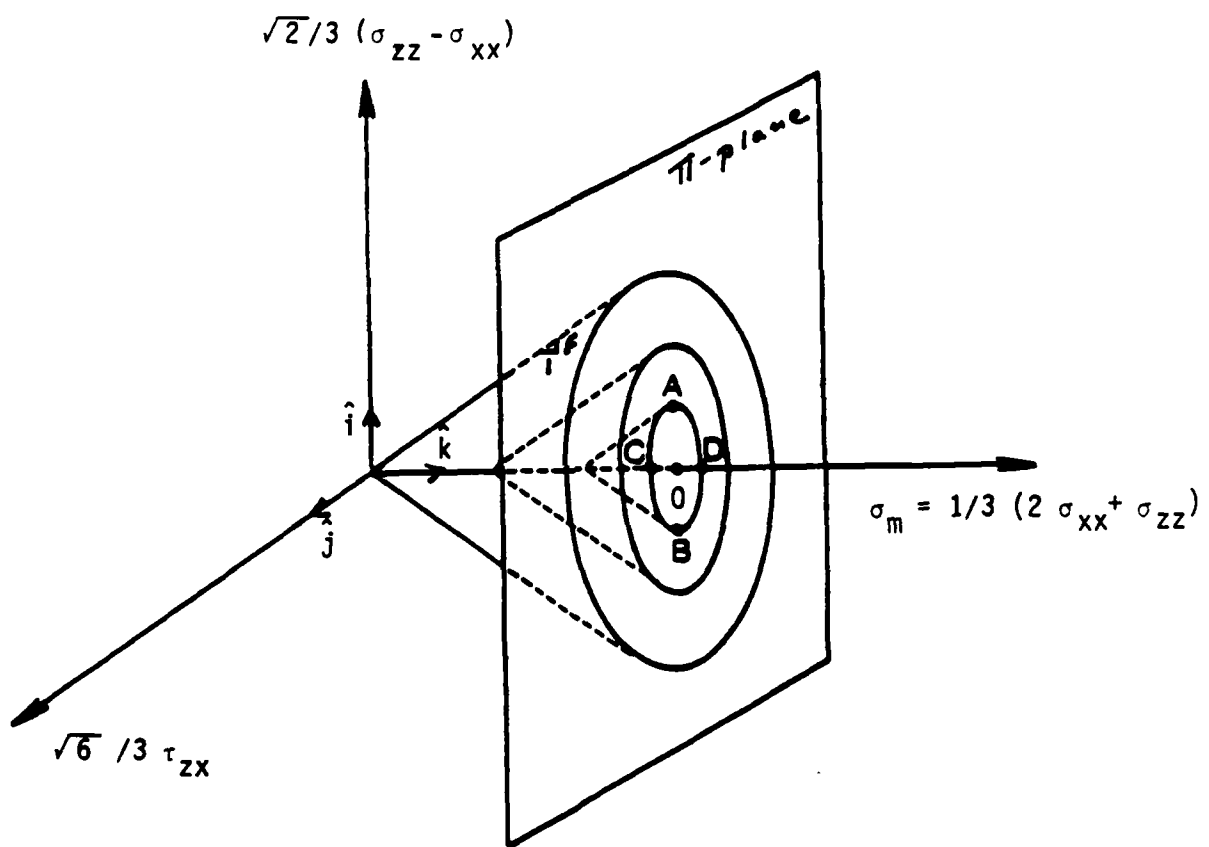


Figure 9. Three-dimensional stress space, yield cones,  $\pi$ -planes, and yield circles, for case  $\sigma_{xx} = \sigma_{yy}$  and  $\tau_{xy} = \tau_{yz} = 0$ .

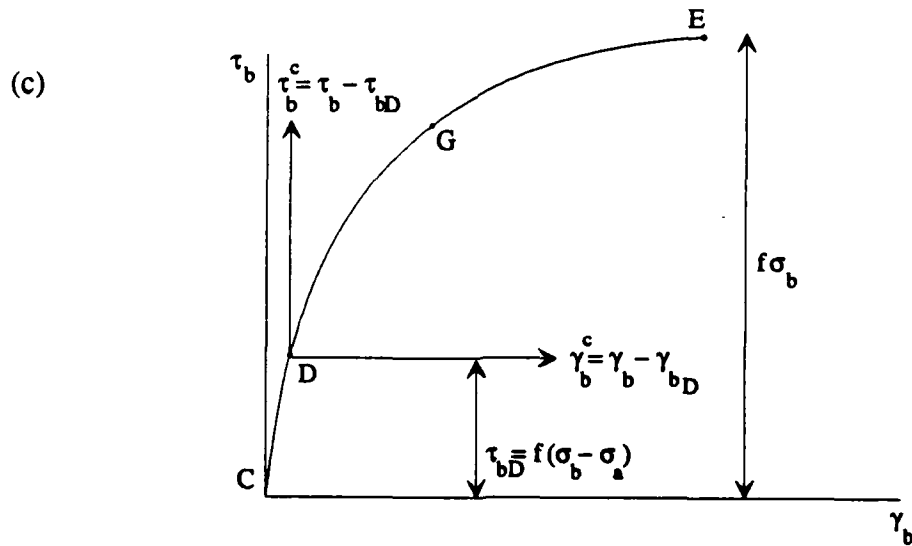
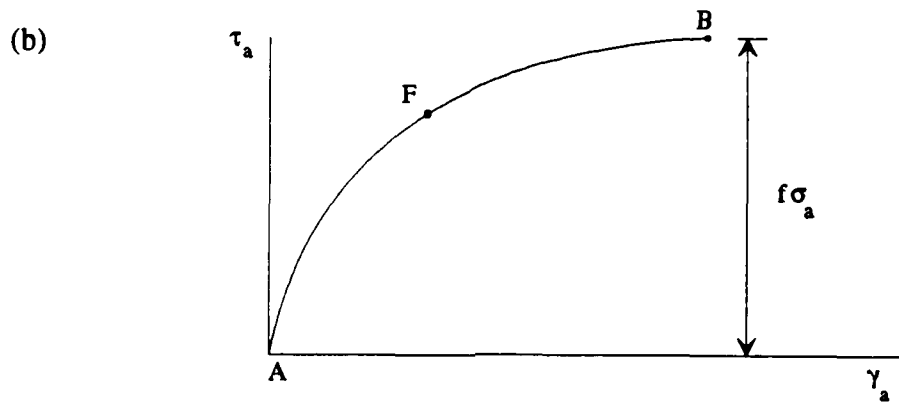
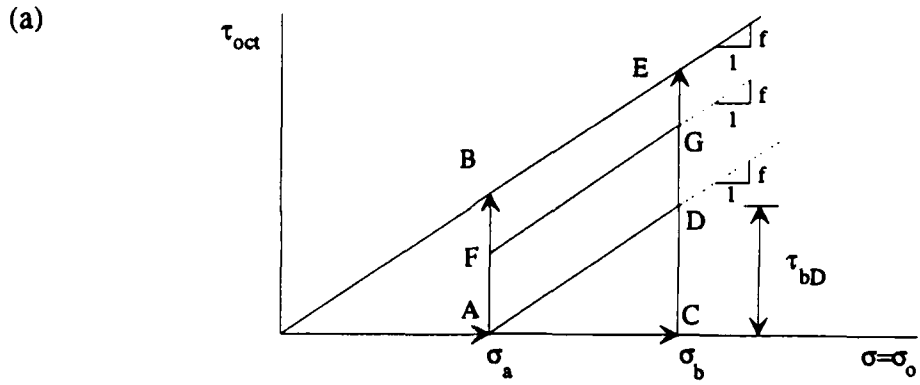


Figure 10. Normalized procedure to compare deviatoric monotonic  $\tau_{oct}$  versus  $\gamma_{oct}$  curves at two different pressures  $\sigma_b > \sigma_a$ . Curve DGE is predicted to be identical to curve AFB.

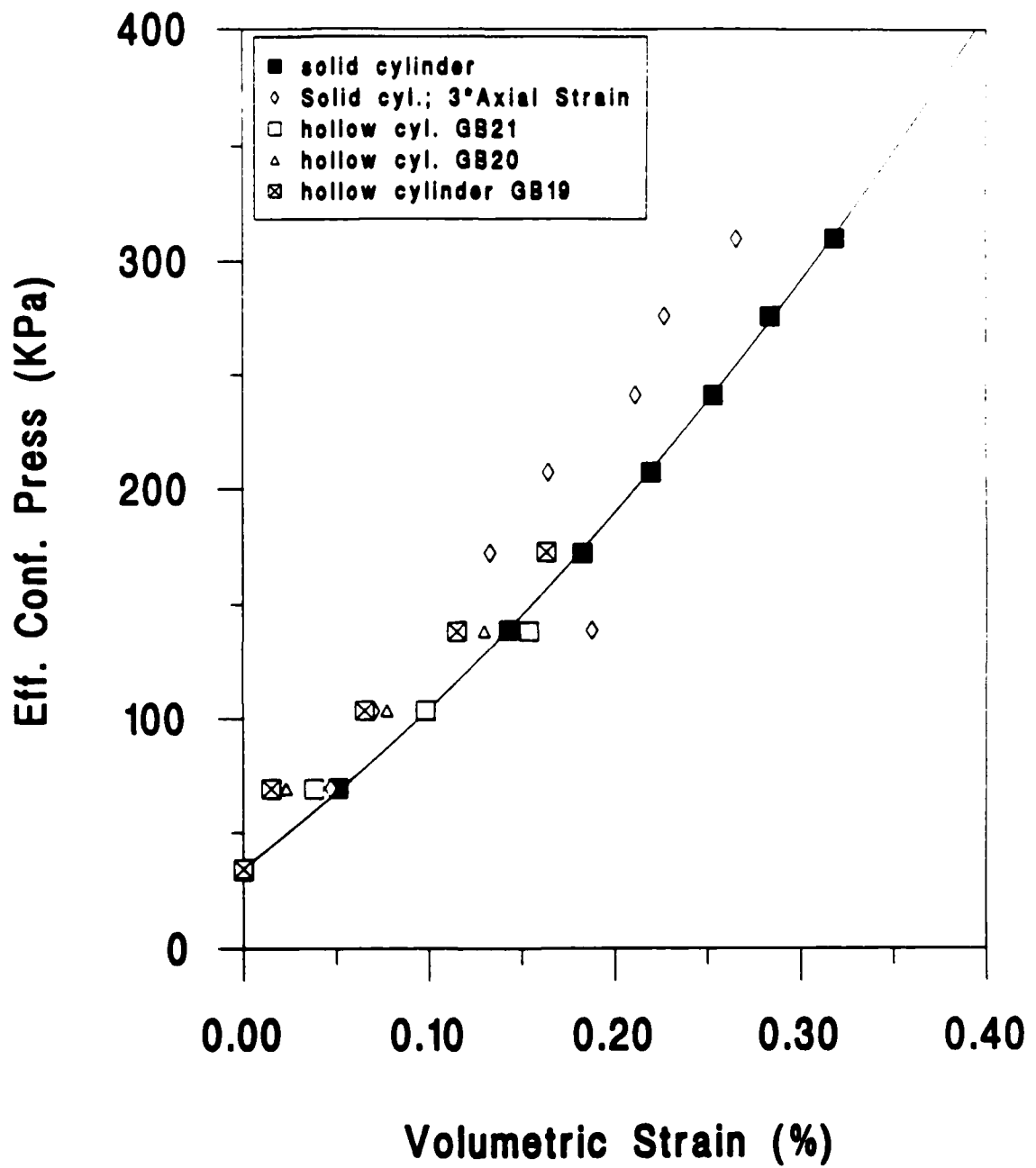


Figure 11. Comparison between volumetric strain obtained under isotropic compression in solid and hollow cylindrical specimens. Data have been corrected for membrane compliance.

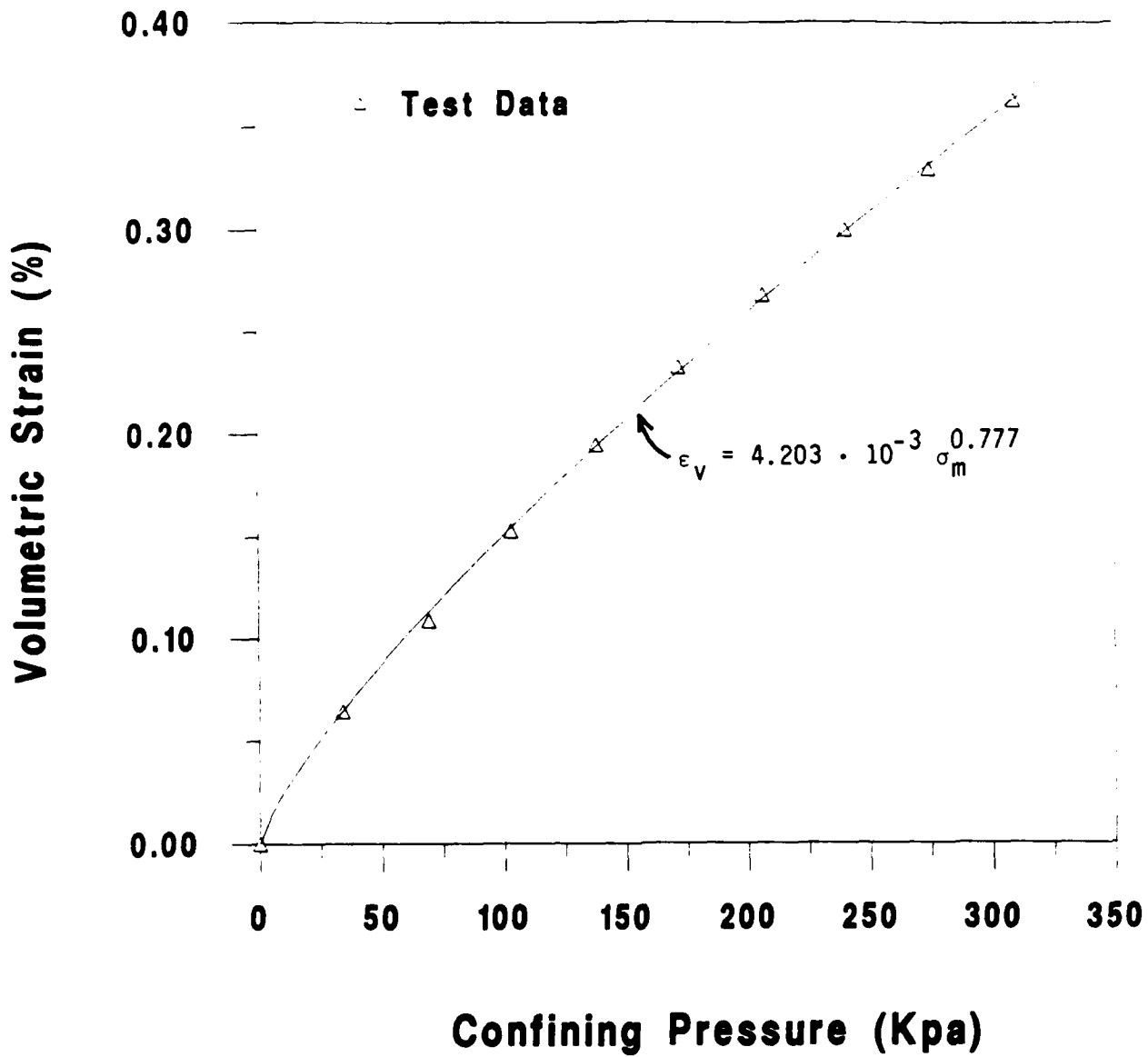


Figure 12. Fitting of equation to measured volumetric strains during isotropic compression, solid cylindrical specimen. Data have been corrected for membrane compliance.

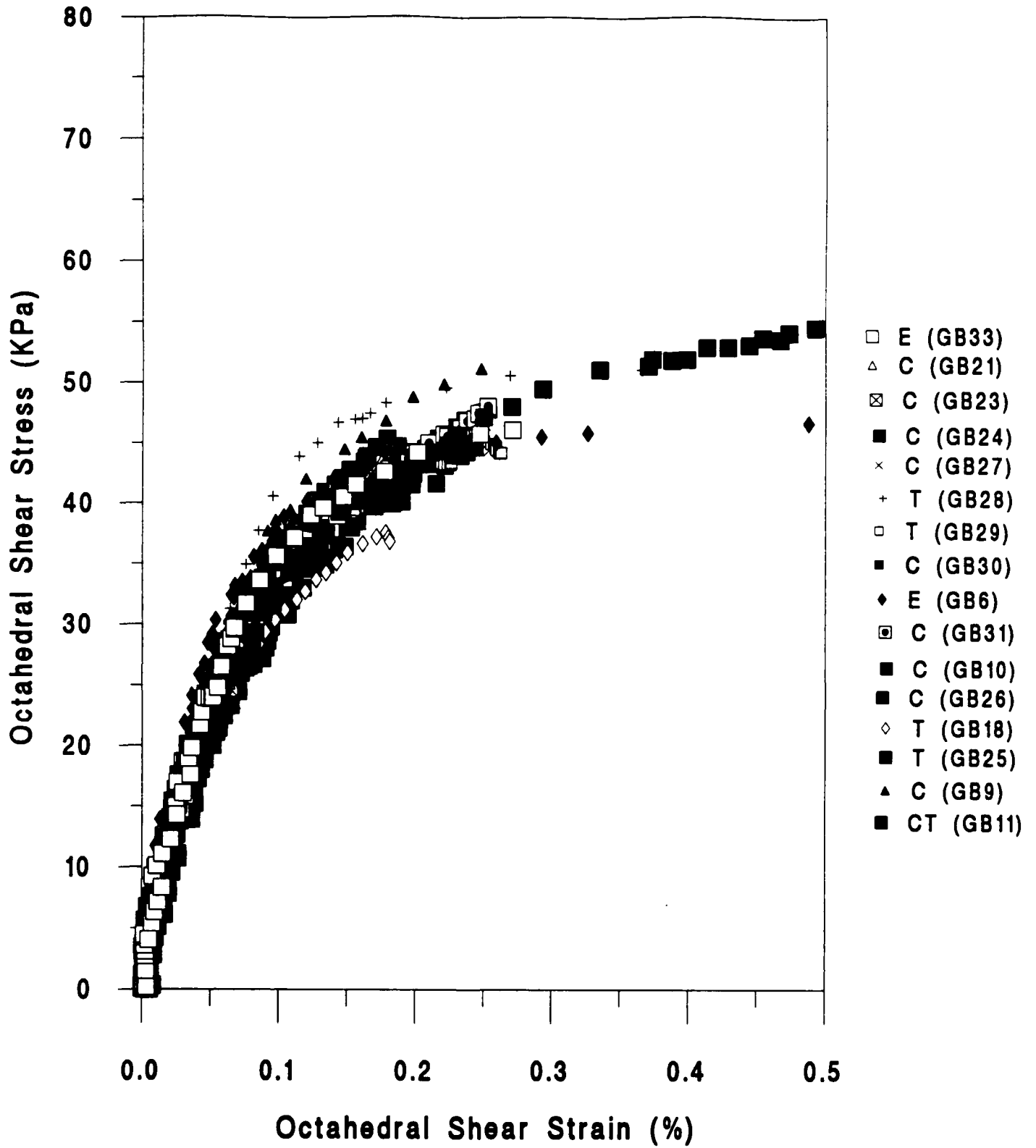


Figure 13. Deviatoric monotonic loading results on hollow cylinder specimens, in compression (C), extension (E), torsion (T), and compression-torsion (CT). All tests are at constant mean pressure,  $\sigma_m = 138$  KPa.

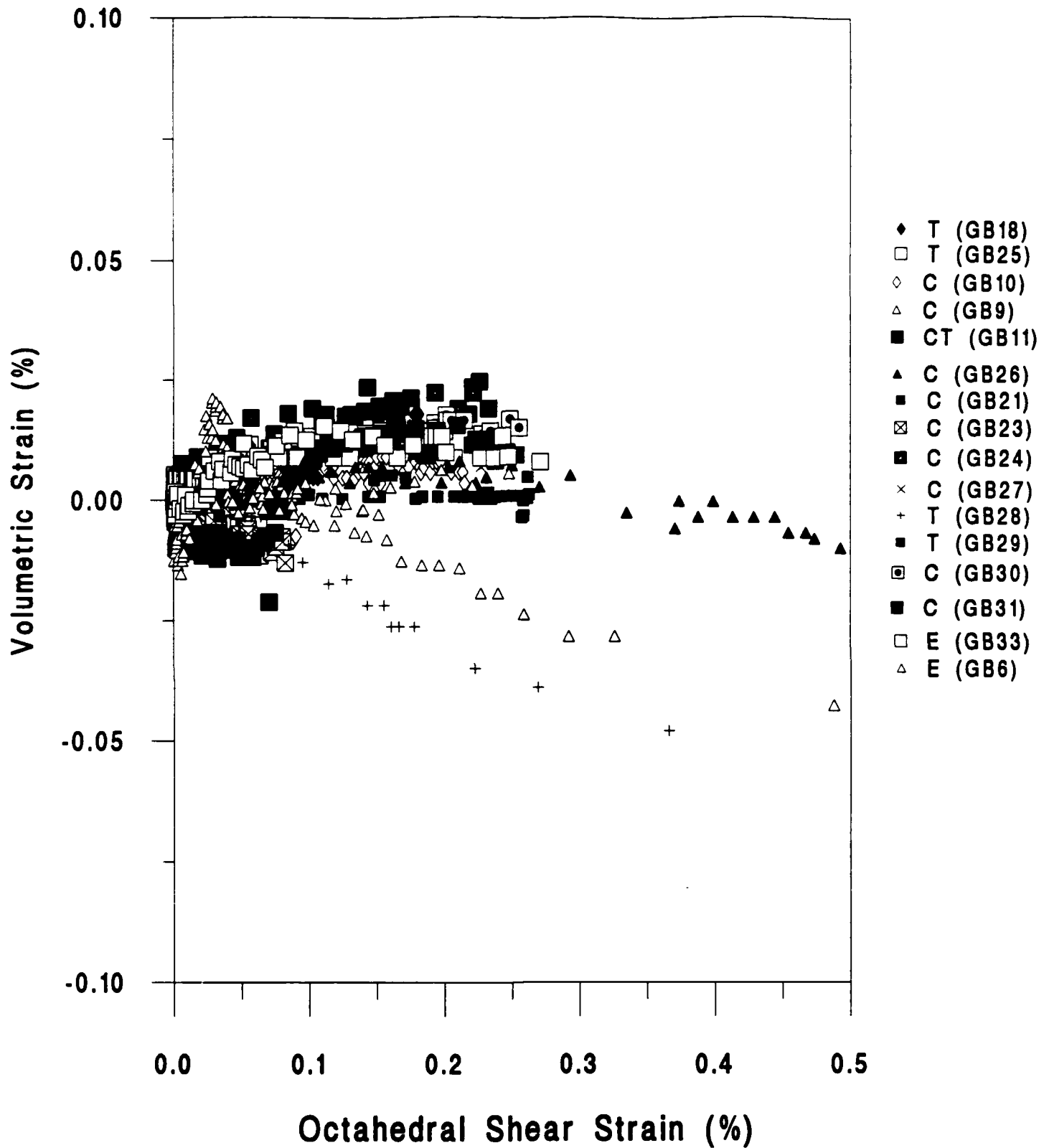


Figure 14. Volumetric strains measured in same tests of Fig. 13,  $\sigma_m = 138$  KPa.

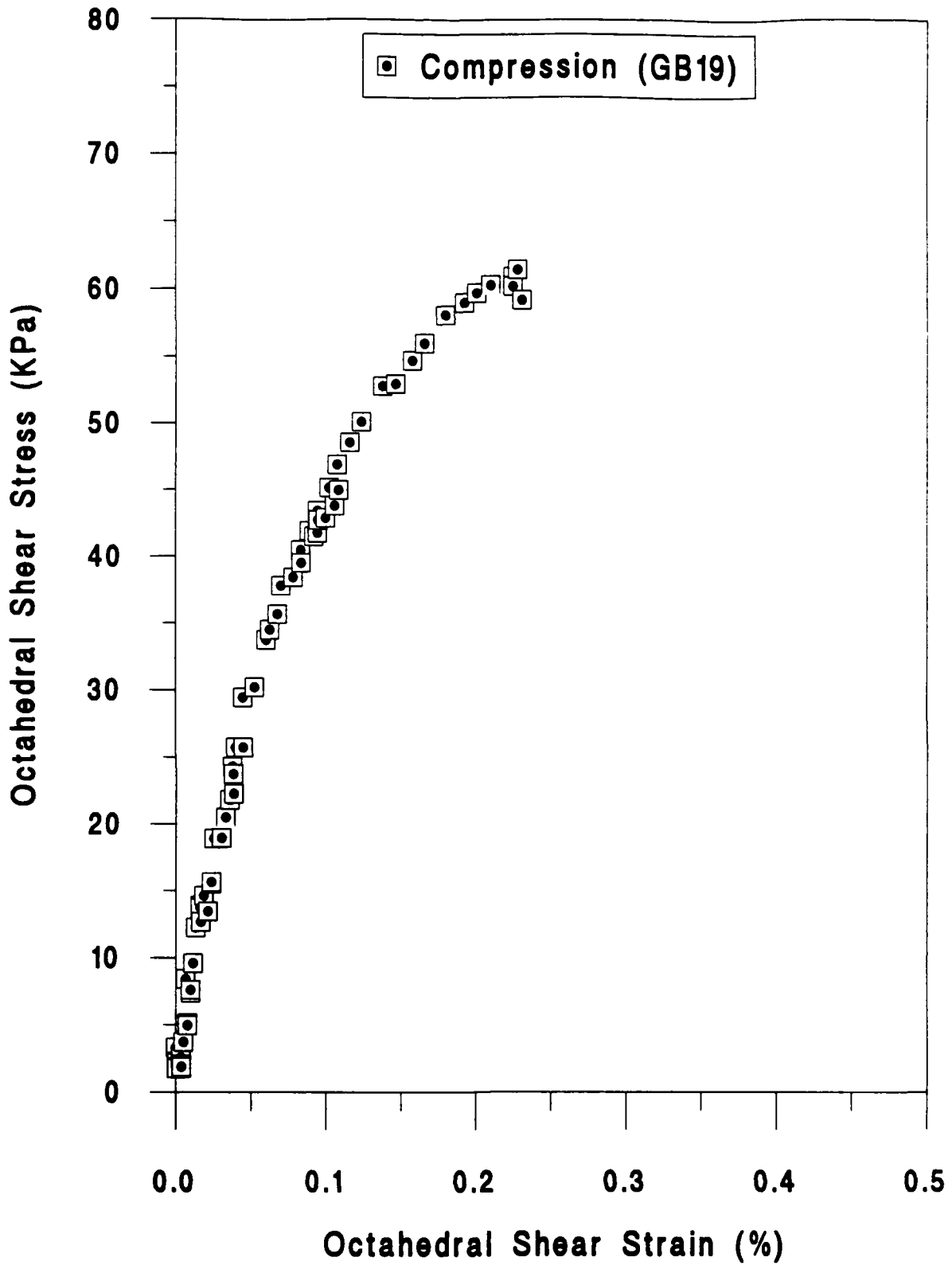


Figure 15. Deviatoric monotonic compression loading test GB19, on hollow cylinder specimen, constant mean pressure,  $\sigma_m = 180$  KPa.

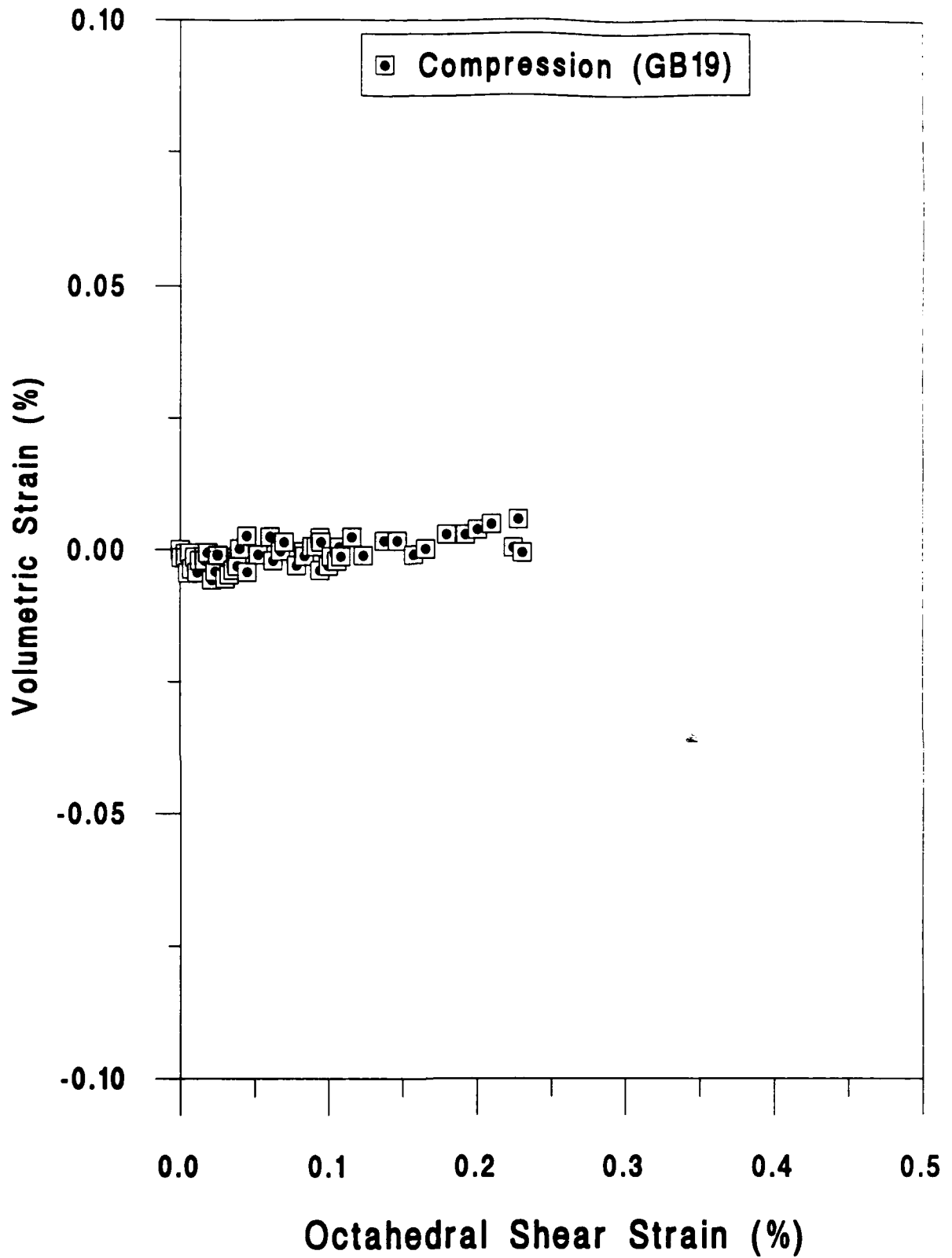


Figure 16. Volumetric strains measured in compression test GB19, hollow cylinder specimen, constant mean pressure,  $\sigma_m = 180$  KPa.

### Compression Test GB27 Beginning of Loading

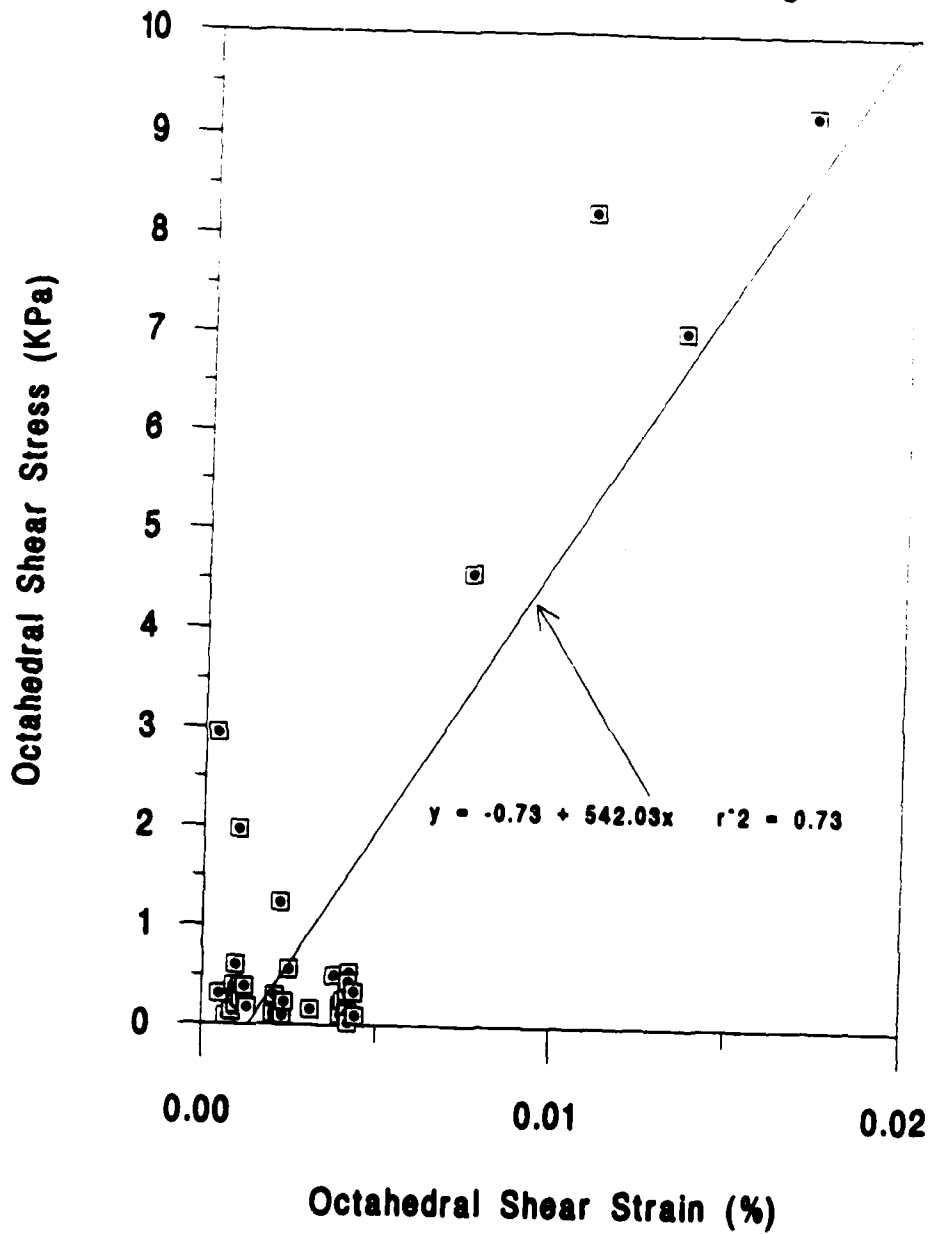


Figure 17. Calculation of  $G_0$  at beginning of deviatoric test GB27,  
 $\sigma_m = 138$  KPa ( $G_0 = 5.42 \cdot 10^4$  KPa).

### Torsion Test GB28 Beginning of Loading

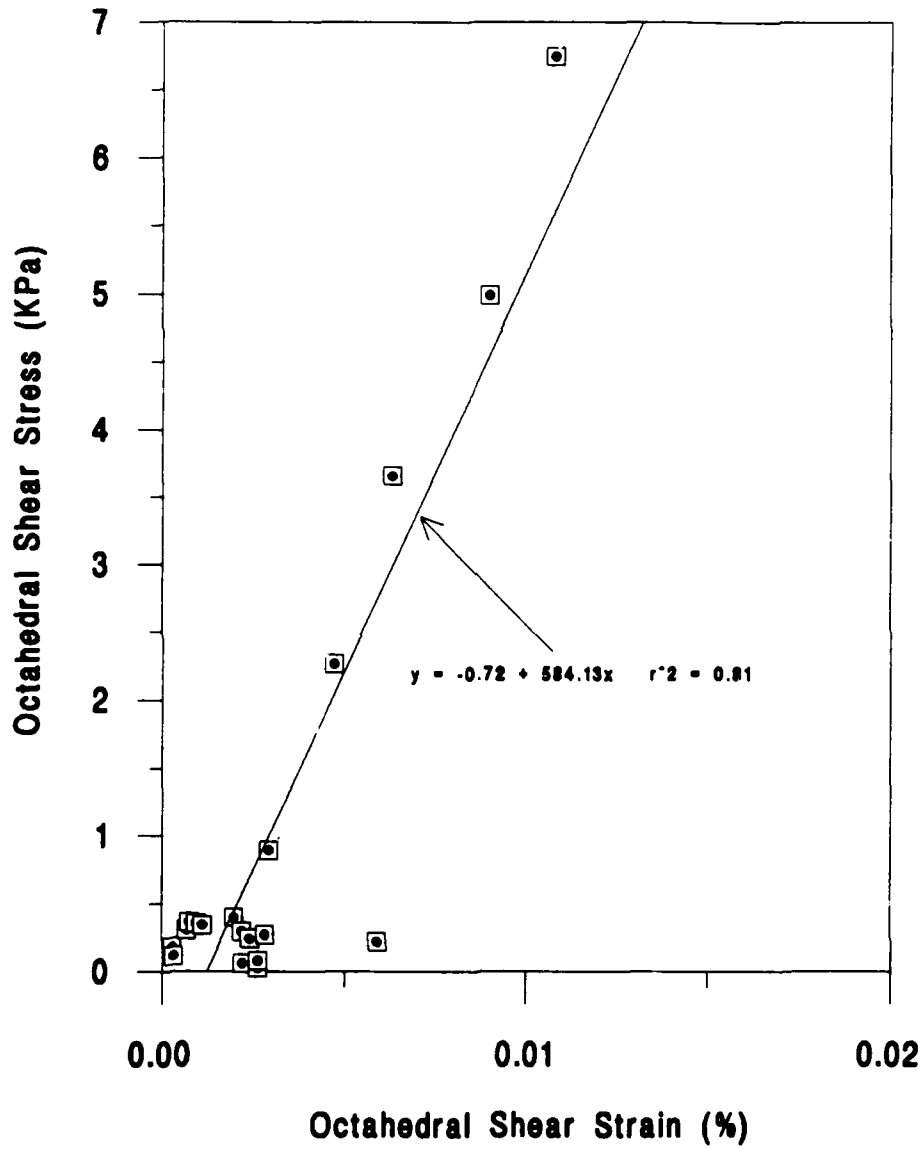


Figure 18. Calculation of  $G_0$  at beginning of deviatoric test GB28,  
 $\sigma_m = 138$  KPa ( $G_0 = 5.84 \cdot 10^4$  KPa).

# Compression Test GB19 (180 KPa) Beginning of Loading

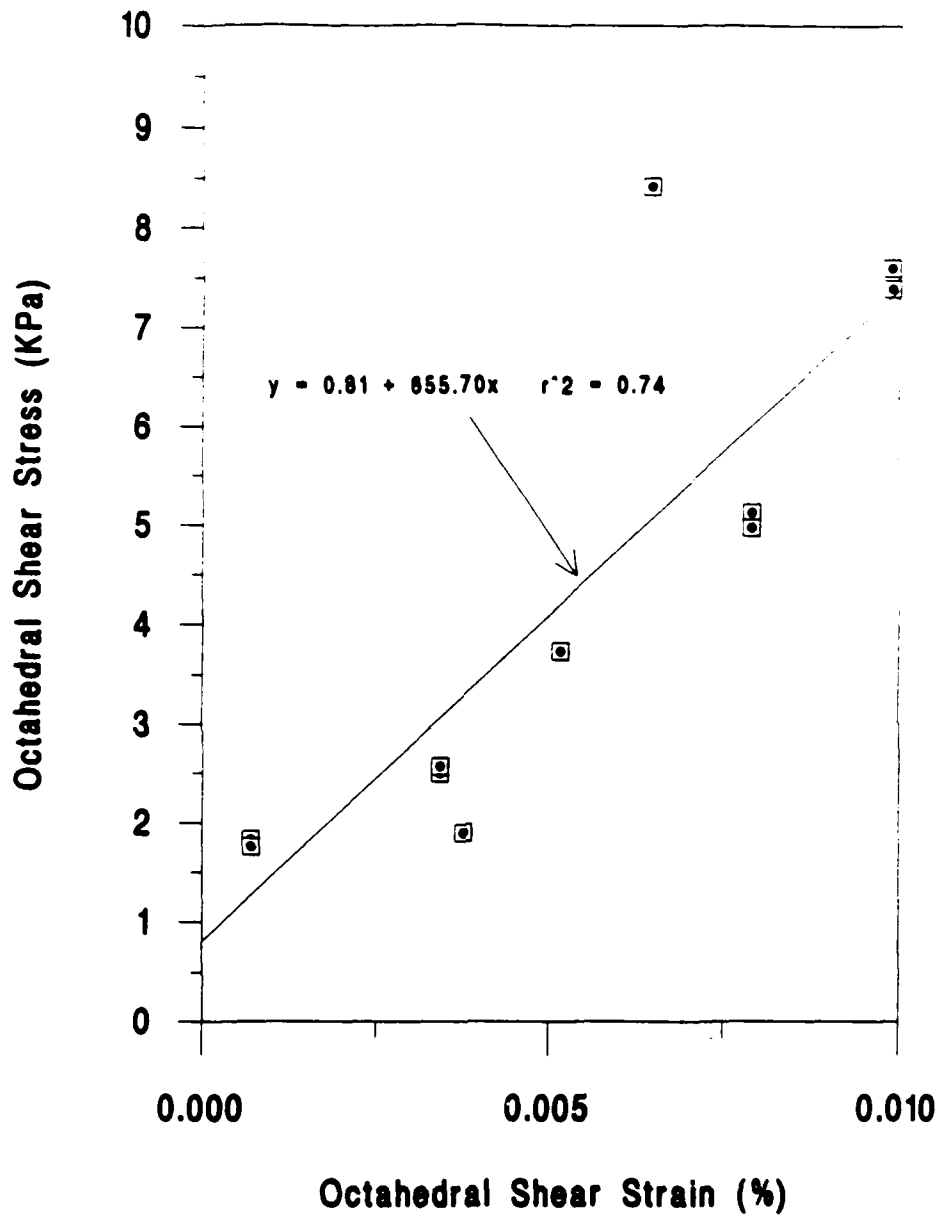


Figure 19. Calculation of  $G_0$  at beginning of deviatoric test GB19,  $\sigma_m = 180$  KPa ( $G_0 = 6.55 \cdot 10^4$  KPa).

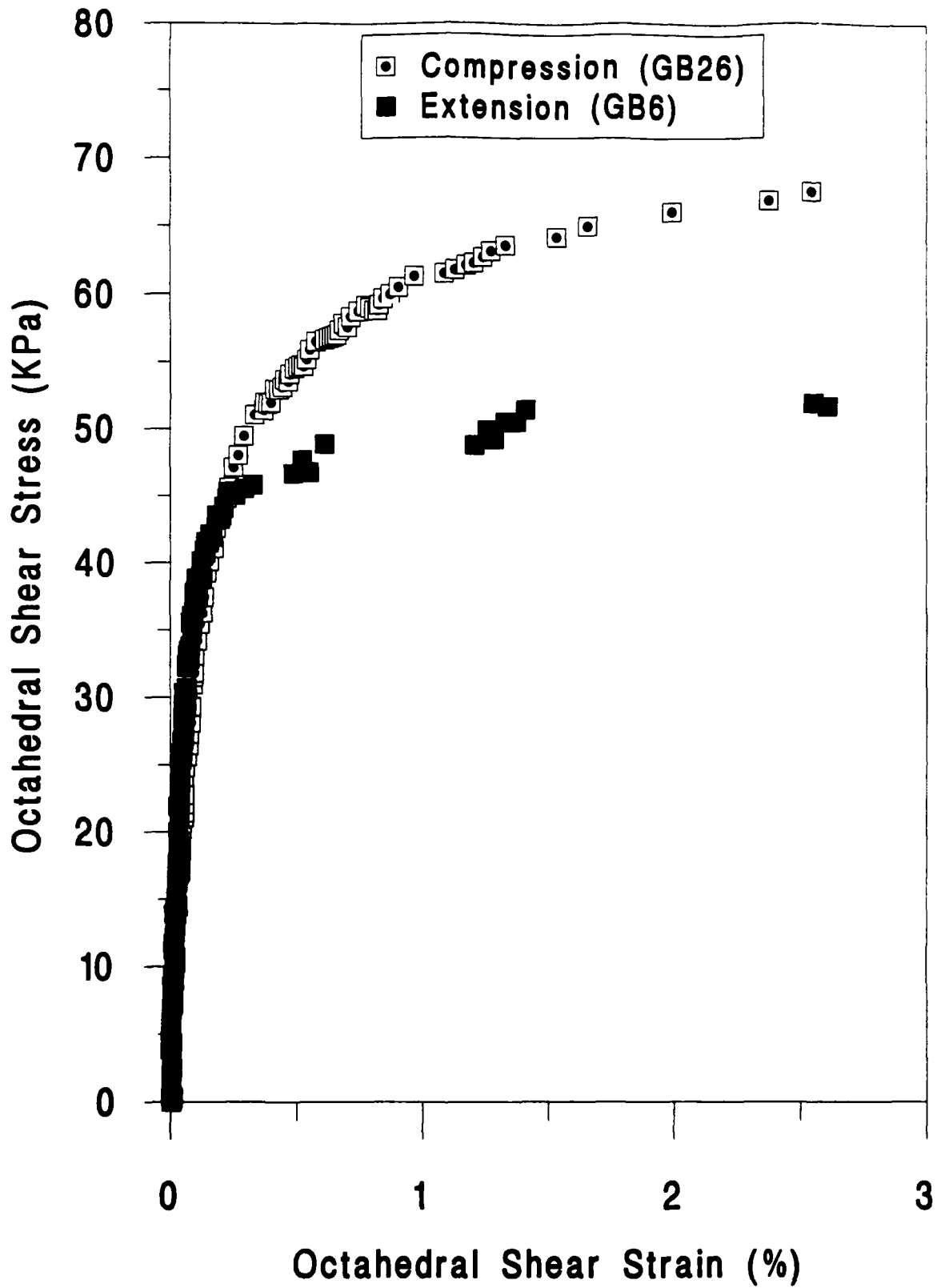


Figure 20. Deviatoric monotonic compression and extension loading to failure, hollow cylinder specimens, constant mean pressure,  $\sigma_m = 138$  KPa.

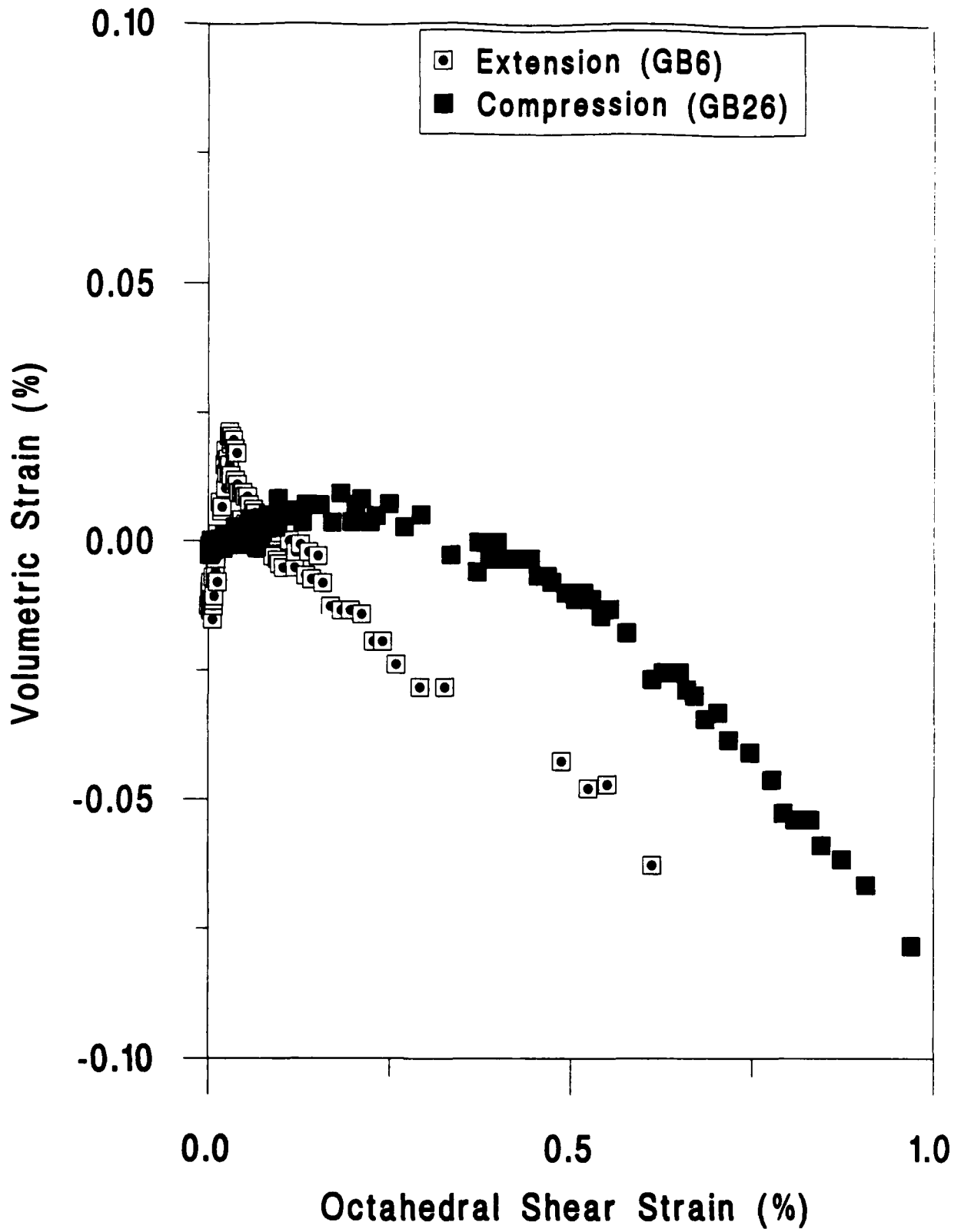


Figure 21. Volumetric strains measured in same tests of Fig. 20,  $\sigma_m = 138$  KPa.

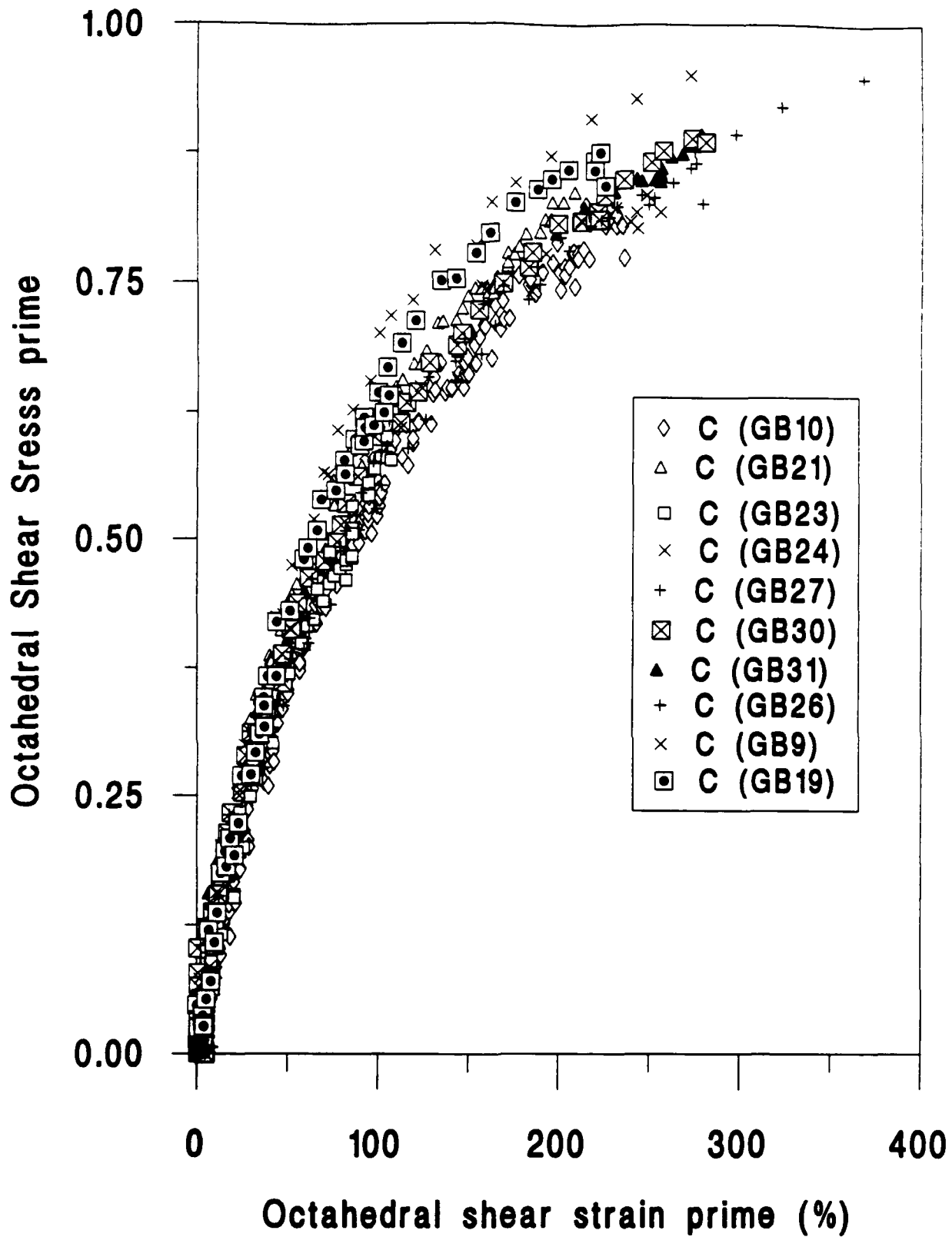


Figure 22.  $\tau'_{oct} = \tau_{oct}/(f \sigma_m)$  versus  $\gamma'_{oct} = (G_0/f \sigma_m) \gamma_{oct}$  for compression tests on hollow cylinder specimens at different values of  $\sigma_m$ . Test GB19 is at  $\sigma_m = 180$  KPa; all other tests correspond to  $\sigma_m = 138$  KPa.

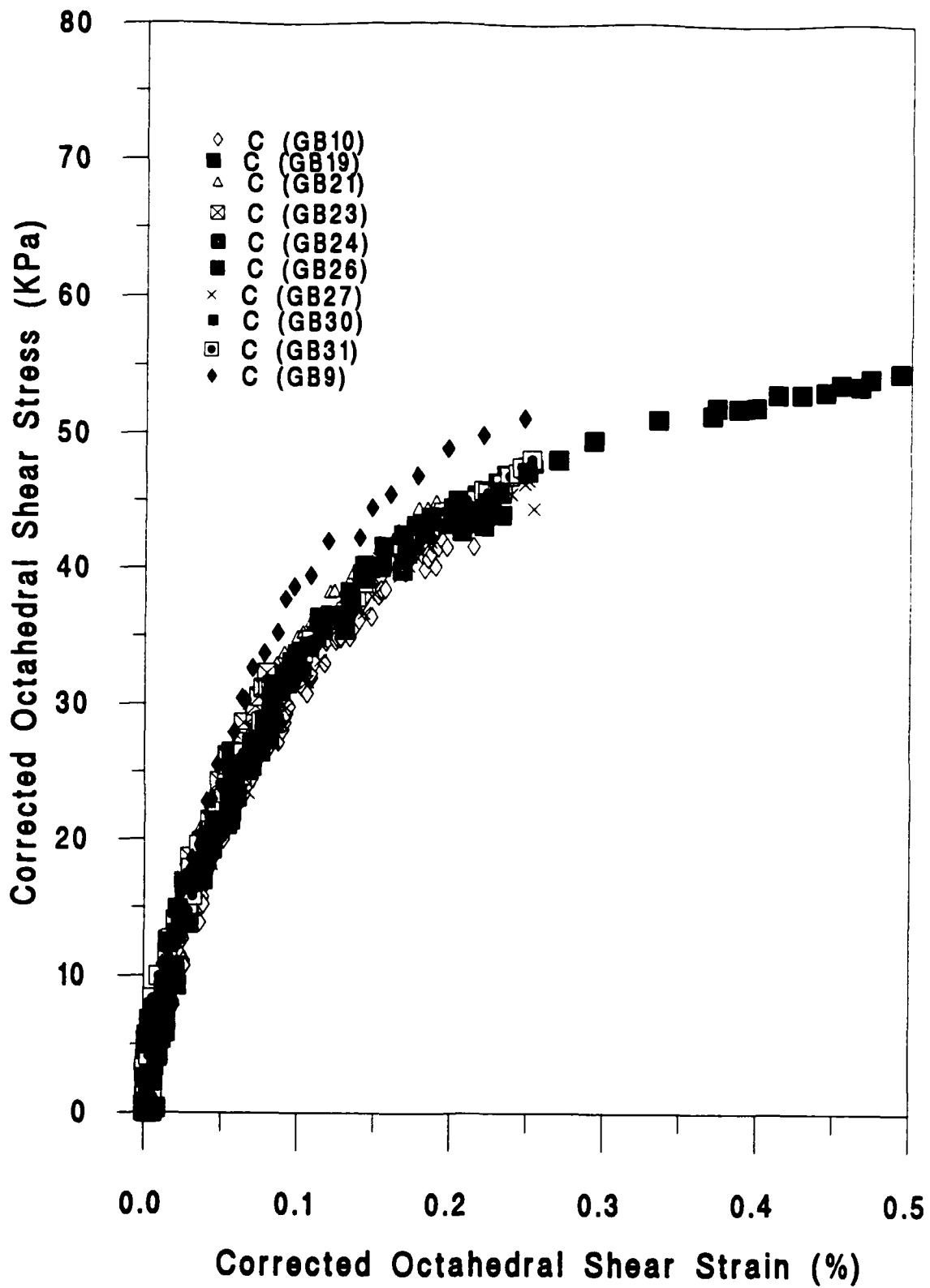


Figure 23.  $\tau^C$  versus  $\gamma^C$  for compression tests on hollow cylinder specimens at different values of  $\sigma_m$ . For test GB19 ( $\sigma_m = 180$  KPa),  $\tau^C$  and  $\gamma^C$  were obtained as shown in Fig. 10. For all other tests ( $\sigma_m = 138$  KPa),  $\tau^C = \tau_{oct}$  and  $\gamma^C = \gamma_{oct}$ .

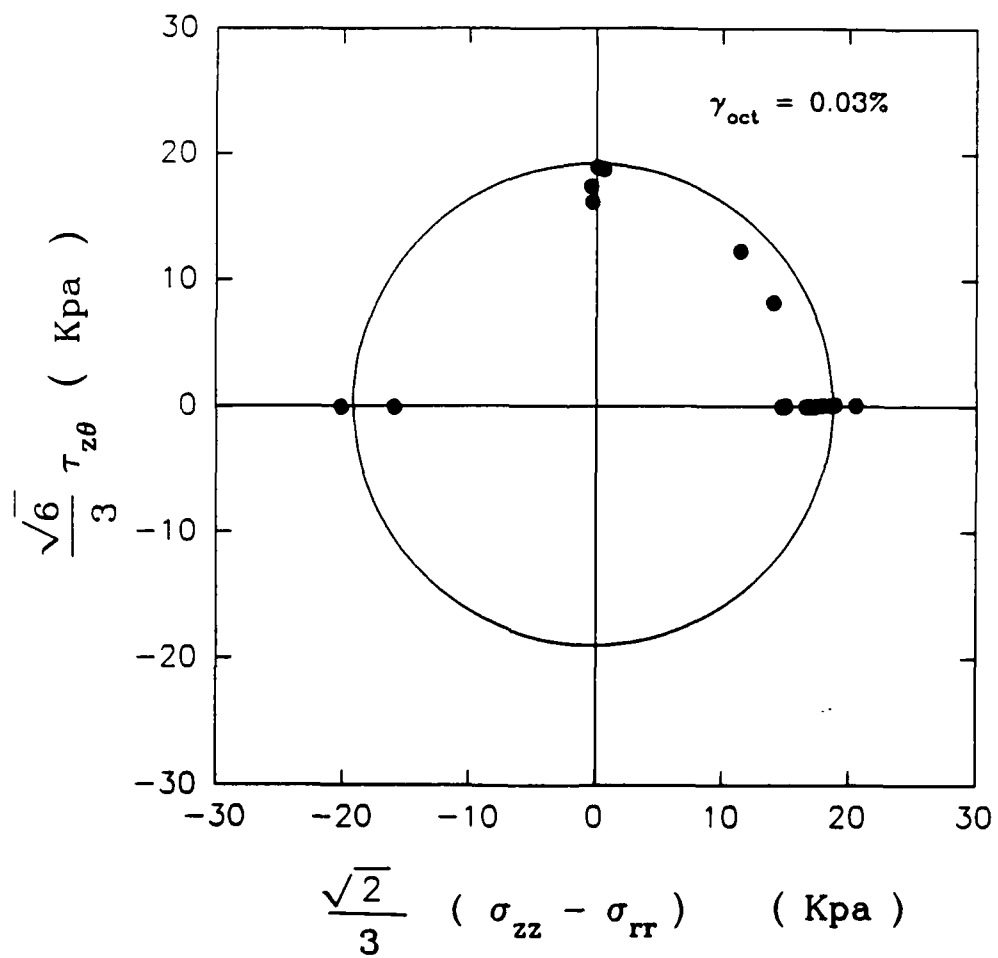


Figure 24. Initial yield locus determined from all deviatoric monotonic loading tests with constant  $\sigma_m = 138$  KPa.

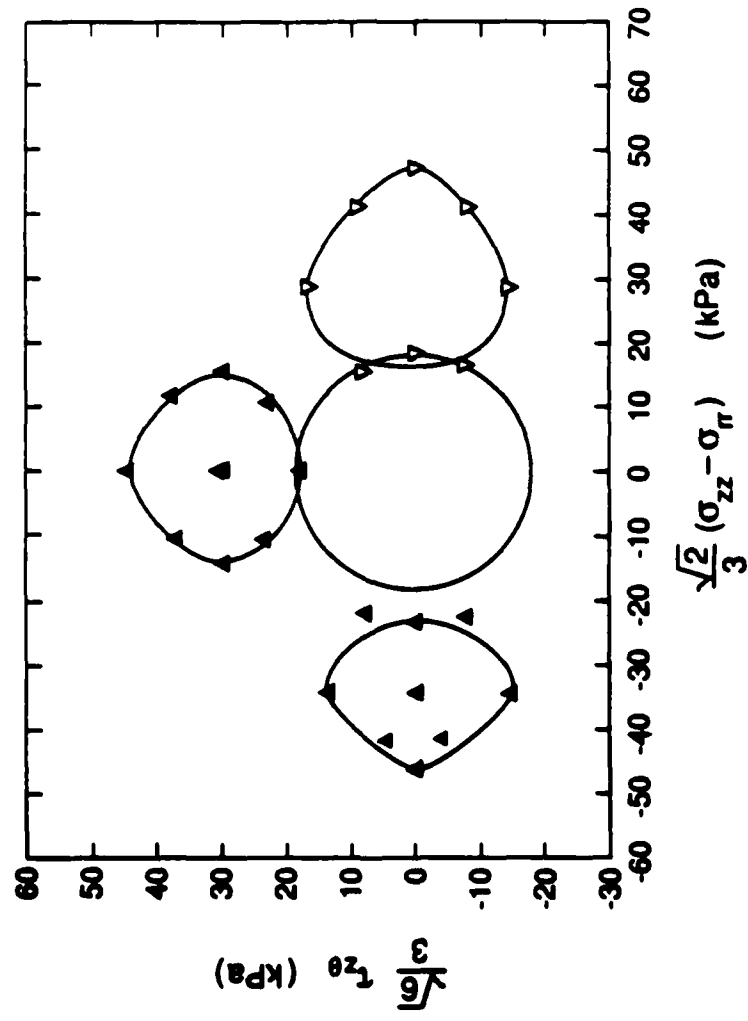


Figure 25. Initial and subsequent yield loci (after prestraining to  $\gamma_{oct} = 0.25\%$ ) for compression, extension and torsion tests GB29, GB30, GB31, hollow cylinder specimens, constant mean stress,  $\sigma_m = 138$  KPa.

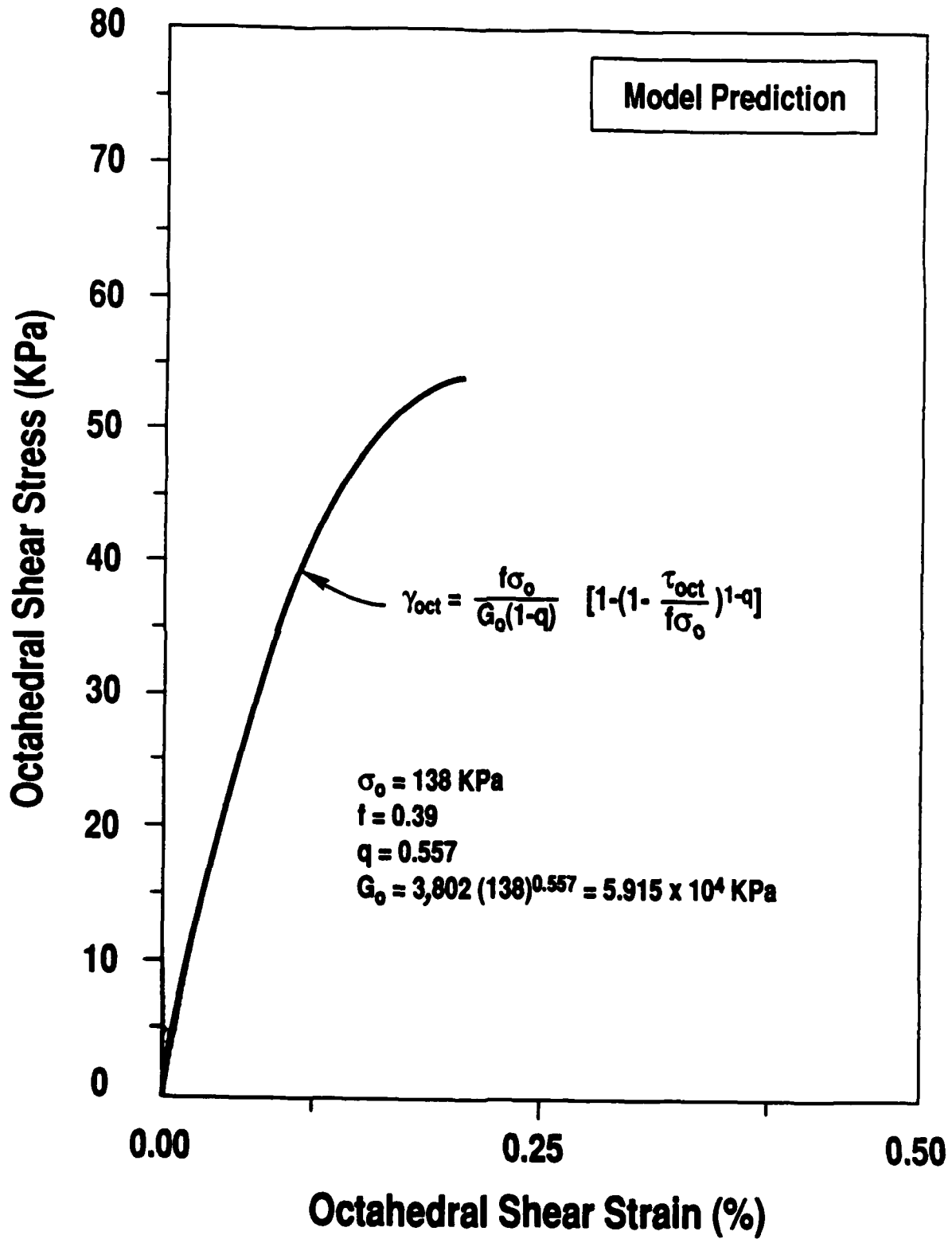


Figure 26. Deviatoric stress-strain curve predicted by model for constant mean stress loading,  $\sigma_m = 138 \text{ KPa}$ .

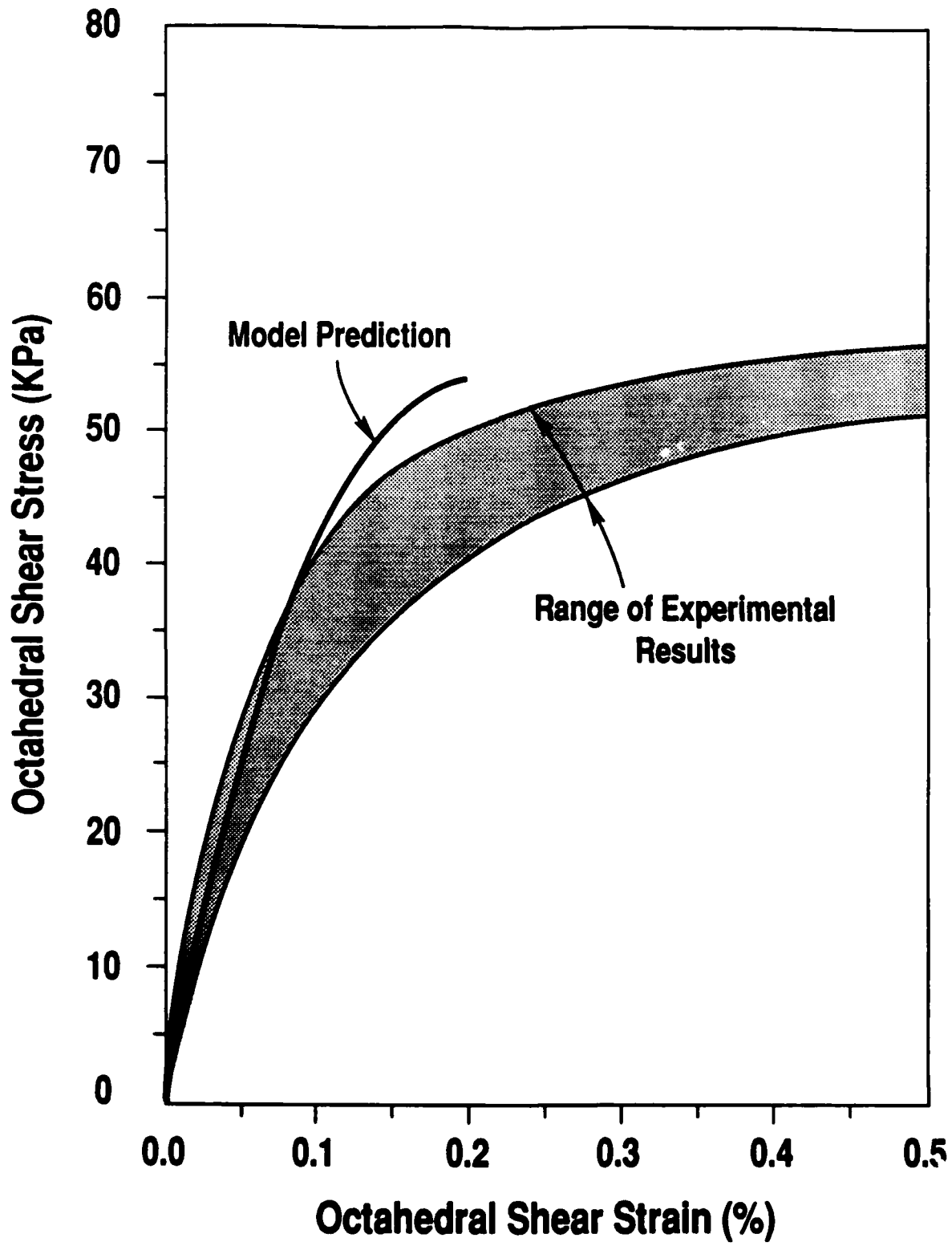


Figure 27. Comparison between model prediction and experimental results,  $\sigma_m = 138$  KPa.

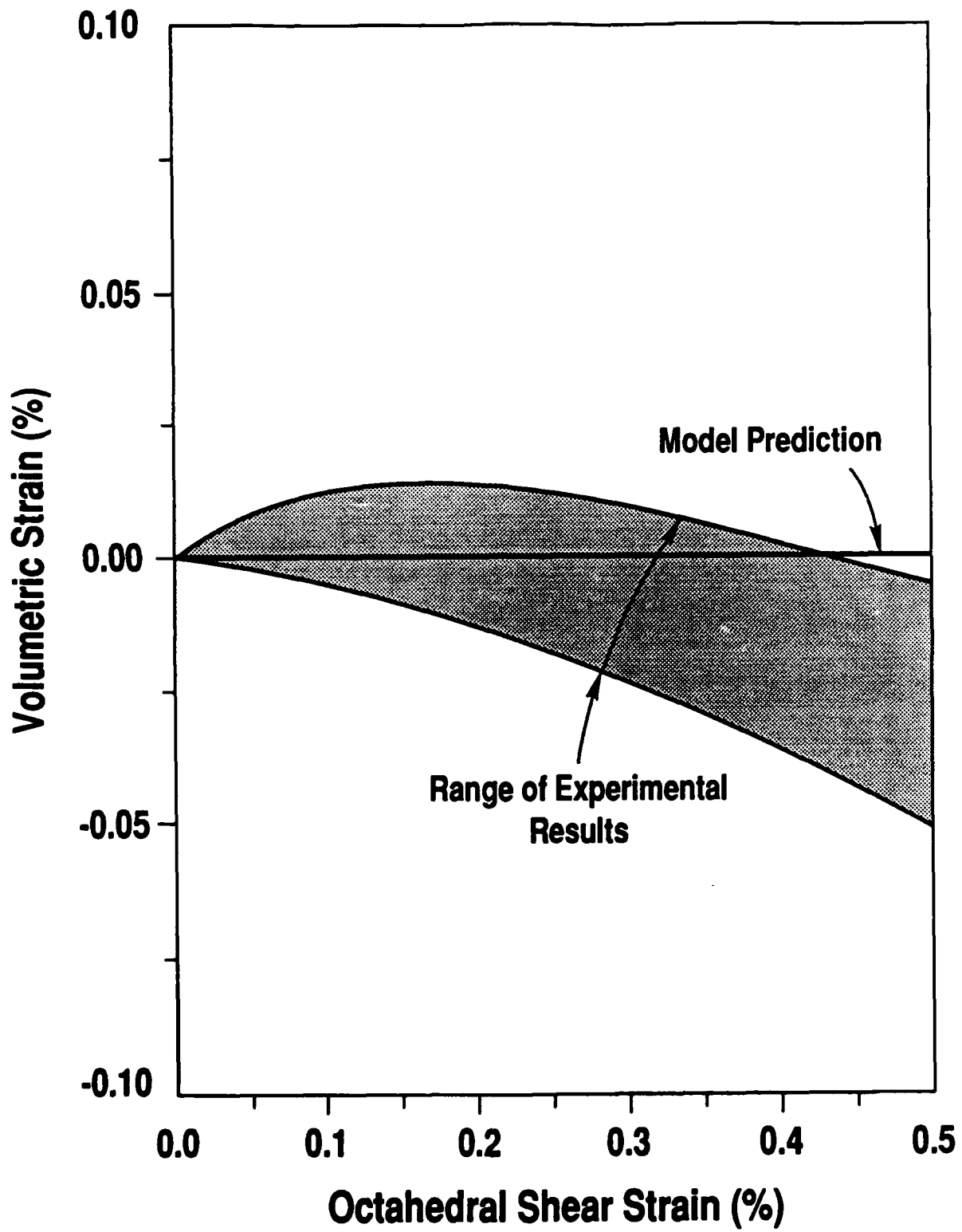


Figure 28. Comparison between model prediction and experimental results,  $\sigma_m = 138$  KPa.

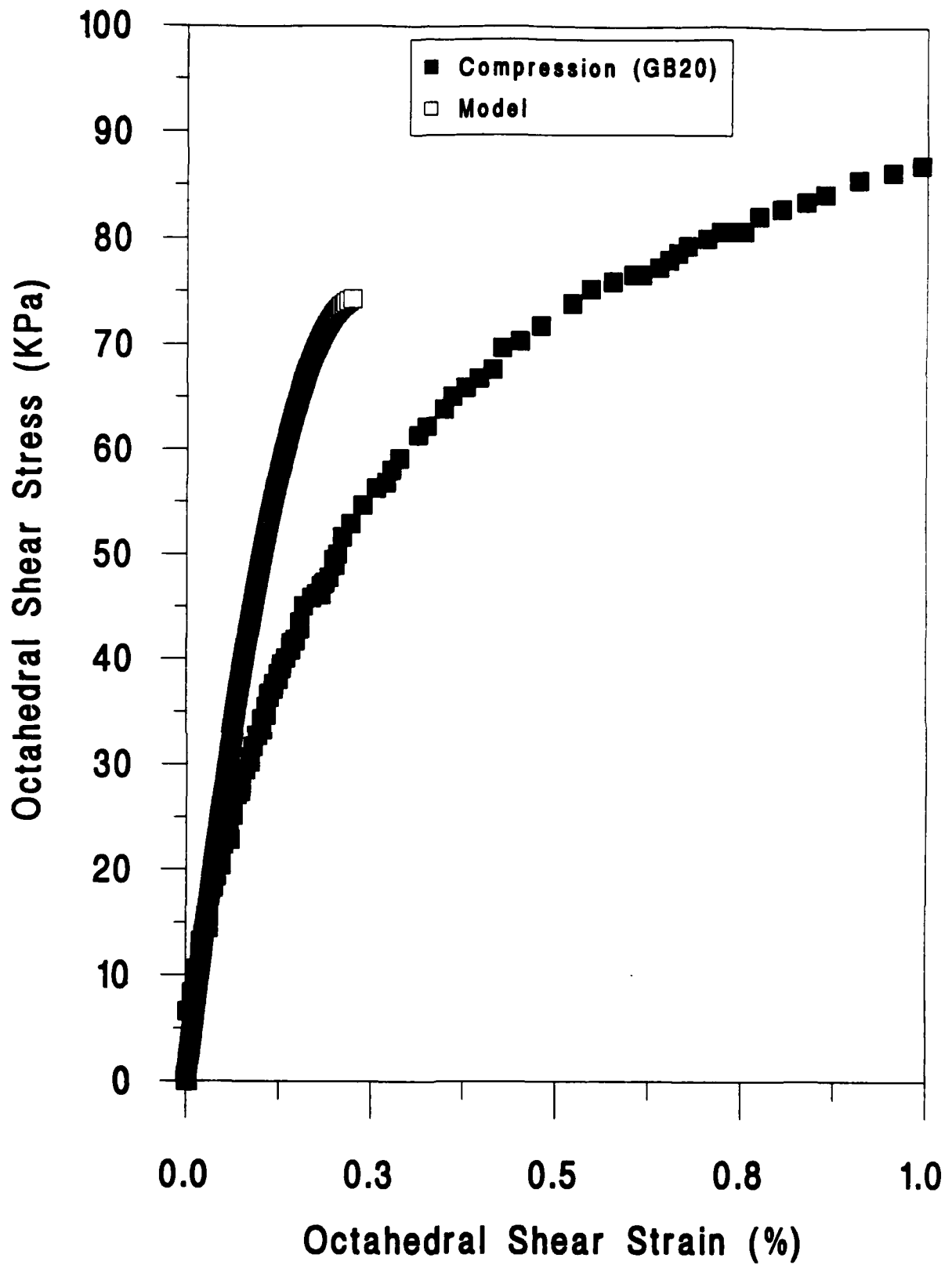


Figure 29. Comparison between model prediction and experimental results, triaxial compression test GB20 (cell pressure = 138 KPa).

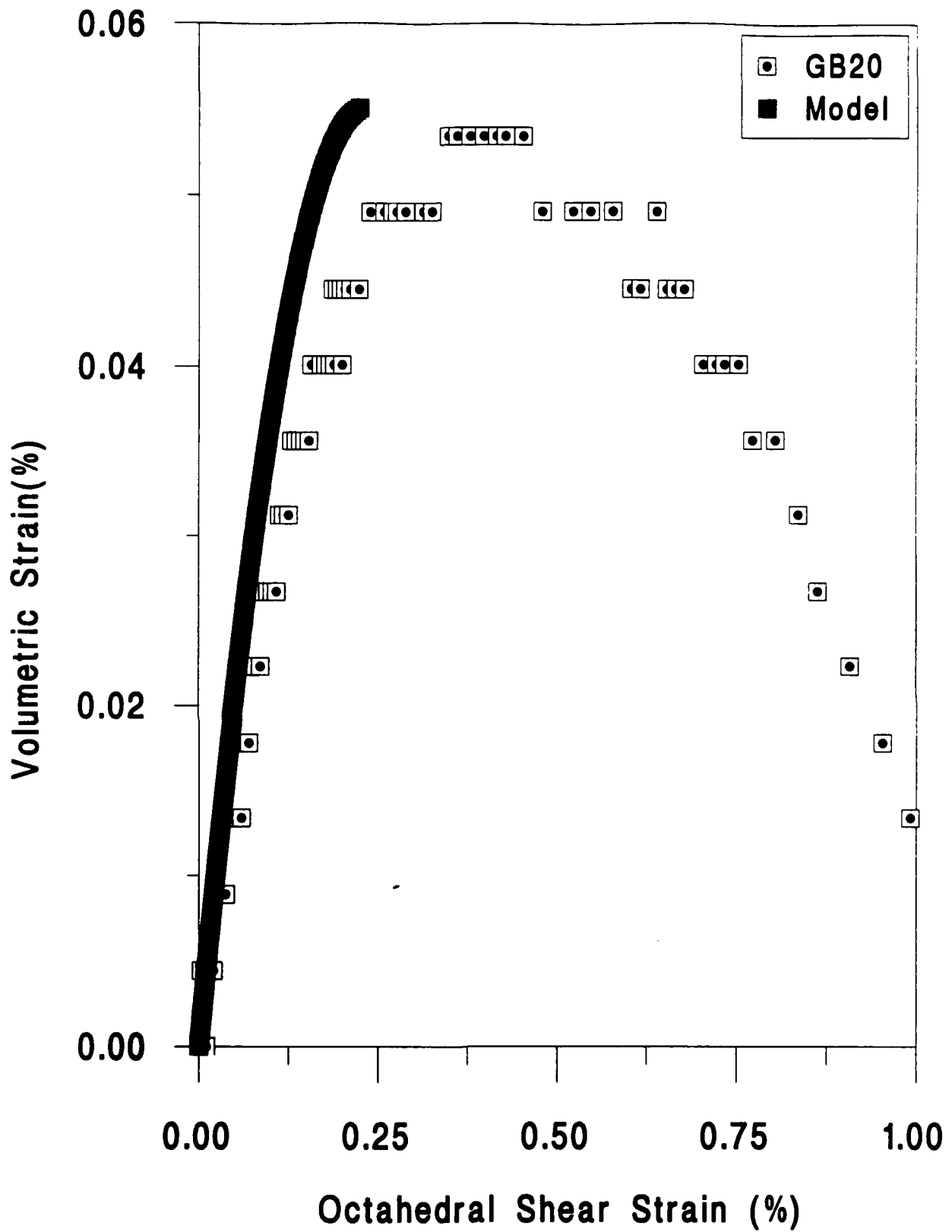


Figure 30. Comparison between model prediction and experimental results, triaxial compression test GB20 (cell pressure = 138 KPa).

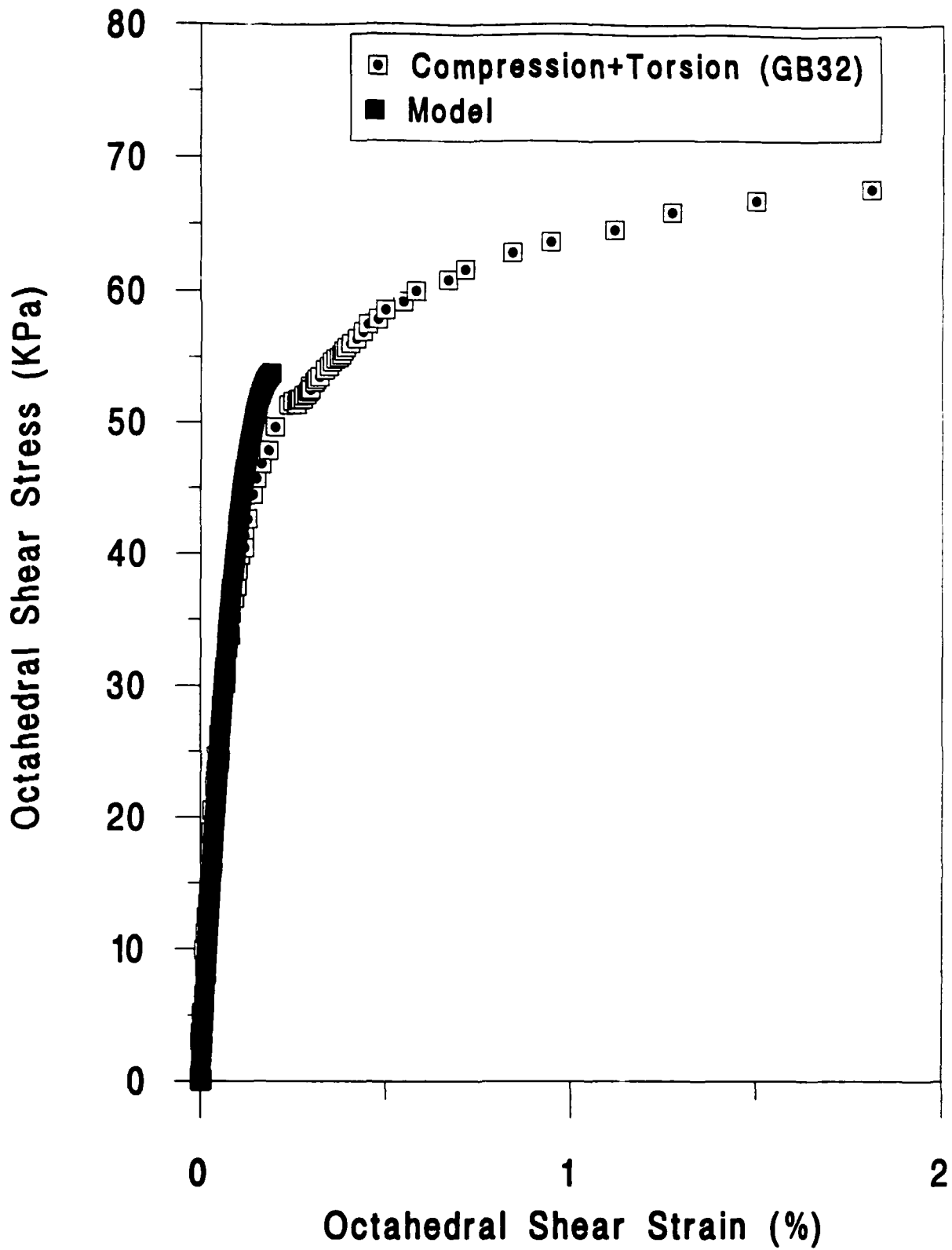


Figure 31. Comparison between model qualitative simulation and compression and torsion test GB32,  $\sigma_m = 138$  KPa.

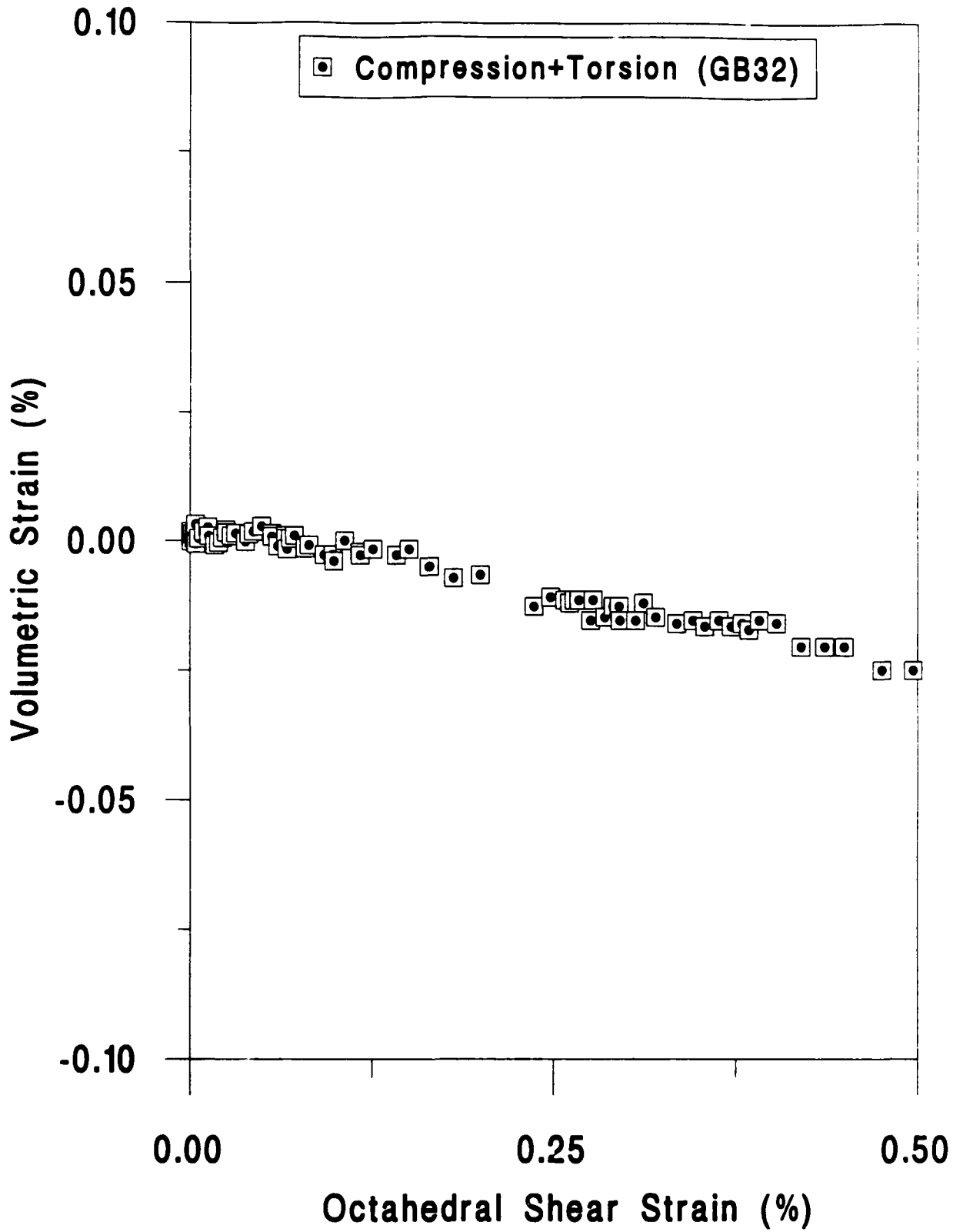


Figure 32. Measured volumetric strains in compression and torsion test GB32,  $\sigma_m = 138$  KPa.